3-2020

Spacecraft Position Estimation and Attitude Determination using Terrestrial Illumination Matching

Liberty M. Shockley

Spacecraft Position Estimation and Attitude Determination using Terrestrial Illumination Matching

THESIS

Liberty M. Shockley, Second Lieutenant, USAF

AFIT-ENY-MS-20-M-280

DEPARTMENT OF THE AIR FORCE
AIR UNIVERSITY

AIR FORCE INSTITUTE OF TECHNOLOGY

Wright-Patterson Air Force Base, Ohio

AFIT-ENY-MS-20-M-280

Spacecraft Position Estimation and Attitude Determination using Terrestrial Illumination Matching

THESIS

Presented to the Faculty

Department of Aeronautics and Astronautics

Graduate School of Engineering and Management

Air Force Institute of Technology

Air University

Air Education and Training Command

in Partial Fulfillment of the Requirements for the

Degree of Master of Science in Astronautical Engineering

Liberty M. Shockley, BS

Second Lieutenant, USAF

26 March 2020

AFIT-ENY-MS-20-M-280

Spacecraft Position Estimation and Attitude Determination using Terrestrial Illumination Matching

Liberty M. Shockley, BS
Second Lieutenant, USAF

Approved:

Maj Robert Bettinger, PhD (Chairman)	Date
Maj Joshuah Hess, PhD (Member)	Date
Maj Constantinos Zagaris, PhD (Member)	Date

Abstract

An algorithm to conduct spacecraft position estimation and attitude determination via terrestrial illumination matching (TIM) is presented consisting of a novel method that uses terrestrial lights as a surrogate for star fields. Although star sensors represent a highly accurate means of attitude determination with considerable spaceflight heritage, with Global Positioning System (GPS) providing position, TIM provides a potentially viable alternative in the event of star sensor or GPS malfunction or performance degradation. The research defines a catalog of terrestrial light constellations, which are then implemented within the TIM algorithm for position acquisition of a generic spacecraft bus. With the algorithm relying on terrestrial lights rather than the established standard of star fields, a series of sensitivity studies are showcased to determine performance during specified operating constraints, to include varying orbital altitude and cloud cover conditions. The pose is recovered from the matching techniques by solving the epipolar constraint equation using the Essential and Fundamental matrix, and point-to-point projection using the Homography matrix. This is used to obtain relative position change and the spacecraft's attitude when there is a measurement. When there is not, both an extended and an unscented Kalman filter are applied to test continuous operation between measurements. The research is operationally promising for use with each nighttime pass, but filtering is not enough to sustain orbit determination during daytime operations.

Acknowledgements

I would like to say thank you to my advisor, Maj Bettinger, who has been the shining North Star of my graduate school experience, leading me to explore the world and push the boundaries of my own understanding. The many discussions of history, science, law, and family helped build my character alongside our work. A huge amount of gratitude is owed to Maj Hess and Maj Zagaris for graciously always being my second stop with whatever frantic questions or news I had to share. Certainly I would not be in this position in any capacity without my family. My father who recently experienced the joys of AFIT, was always there to fall asleep with one of my navigation textbooks, and my mother who was always there to share a glass of wine, and who signed up to wholly support another Airman in the family. My little brother for bringing me joy and often a better explanation of our universe than I even knew. Finally, to all of my wonderful friends who were not only interested in my wild pursuits, but who cared to join me around the world on my adventures.

Liberty M. Shockley

Contents

Page

List of Figures

Figure Page

Figure Page

List of Tables

List of Symbols

a	semi-major radius
b	semi-minor radius
$\mathbf{C}$	attitude matrix
e	eccentricity
$\hat{\mathbf{e}}$	unit vector of s
$\mathbf{E}$	Essential Matrix
e^2	square of first eccentricity
f	flattening of the planet
f	process nonlinear vector function
$\mathbb{F}$	matrix of linearized dynamics
$\mathbf{F}$	Fundamental matrix
f_c	focal length of camera
g	gravitational acceleration
$\mathbf{H}$	Jacobian of measurement sensitivity
h	observation function
h_E	height of vehicle above Earths surface
$\mathbf{I}$	identity matrix
JD	Julian Day
$\mathbf{K}$	Kalman gain
k	equatorial gravity constant
N	radius of curvature of vertical prime
n	integer number
$\mathbf{P}$	covariance of state
$\mathbf{Q}$	process noise covariance matrix

q_0	equatorial gravity
$\mathbb{R}$	measurement noise covariance matrix
$\mathbf{R}$	rotation matrix between coordinate frames
$\mathbf{r}$	vehicle position
$\mathbf{s}$	measurement from camera to point on earth
$\mathbf{T}$	pose matrix
$\mathbf{t}$	translation
TT	time
$\mathbf{u}$	input vector
$\mathbf{v}$	vehicle velocity
$\mathbf{w}$	measurement noise
$\mathbb{W}$	weights
$\mathbf{x}$	state vector
$\mathbf{X}$	image coordinate
$\mathbf{y}$	measurement
$\mathbf{Y}$	expected measurement
β	reduced latitude
$\mathbf{\Gamma}$	residuals of observations
Δ	change or nutation
ε	obliquity of the ecliptic
ϑ	Greenwich Apparent Sidereal Time
$\varkappa$	filter tuning value
μ	gravitational parameter
σ	accuracy of sensor
$\boldsymbol{\nu}$	residual
φ	latitude

χ	set of sigma points
ψ	longitude
ω	angular rate

Super/subscripts

-	state a priori, but after propagation
+	state a posteriori
0	initial state
c	integer number
CAM	camera frame
E	conditions for the Earth
ECEF	measured with respect to a rotating frame
ECI	measured with respect to an inertial frame
gc	geocentric
gd	geodetic
i	integer index
k	timestep
m	integer number
m	mean
n	integer number
n	normalized
xx	predicted mean covariance
xy	predicted cross covariance
yy	predicted observed covariance

List of Acronyms

AIAA	American Institute of Aeronautics and Astronautics
AFRL	Air Force Research Laboratory
BRIEF	Binary Robust Independent Elementary Features
BRISK	Binary Robust Invariant Scalable Keypoints
CCD	Charge-Coupled Device
DCM	Directin Cosine Matrix
DMSP	Defense Meteorological Satellite Program
DN	Digital Number
DNB	Day Night Band
DoD	Department of Defense
ECEF	Earth Centered Earth Fixed
ECI	Earth Centered Inertial
EKF	Extended Kalman Filter
EOS	Earth Observing System
EOSDIS	EOS Data and Information System
ESA	European Space Agency
ESOC	European Space Operations Centre
ESTEC	European Space Research and Technology Centre
FAST	Features from Accelerated Segment Test
FLANN	Fast Library for Approximate Nearest Neighbors
FOV	Field of View
FREAK	Fast Retina Keypoint
FWHM	Forward Width at Half Maximum

GDP	Gross Domestic Product
GEO	Geostationary Orbit
GNC	Guidance, Navigation, and Controls
GPS	Global Positioning System
GSHHS	Global Self-Consistent Hierarchical High-Resolution Geography
IEEE	Institute of Electronics and Electrical Engineers
IMU	Inertial Measurement Unit
INS	Inertial Navigation System
LEO	Low Earth Orbit
Llh	Latitude, Longitude, Height Above Earth
MSER	Maximally Stable Extremal regions
NASA	National Air and Space Administration
NGDC	National Geophysical Data Center
NOAA	National Oceanic and Atmospheric Administration
NORAD	North American Aerospace Defense Command
NPP	National Polar-orbiting Partnership
O-BRIEF	Oriented Brief
OLI	Operational Land Image
OLS	Operational Linescan System
OpenCV	Open source Computer Vision
ORB	Oriented FAST and Rotated BRIEF
RANSAC	RANdom SAmple Consensus
RIC	Radial, In-track, Cross-track
RV	Space Vehicles Directorate
SDPE	Strategic Development Planning and Experimentation Office
SGP3	Simplified General Perturbations

SIFT	Scale Invariant Feature Transform
STK	Systems Tool Kit
SURF	Speeded Up Robust Features
TIM	Terrestrial Illumination Matching
TLE	Two Line Element
UKF	Unscented Kalman Filter
USAF	United States Air Force
USGS	United States Geological Survey
VIIRS	Visible Infrared Imaging Radiometer Suite
VNIR	Visible Near Infrared
2BP	2 Body Problem
6DOF	6 Degree of Freedom

Spacecraft Position Estimation and Attitude Determination using Terrestrial Illumination Matching

I. Introduction

City lights are capturing the attention of everyone around the world. They seem to be a fascinating projection of the stars on our Earth, but that can reveal the conditions we experience in our daily lives. People love to follow astronauts on Twitter to see their selfies in the International Space Station's cupola flying 200 miles above our beloved cities. Other than admiring their intrinsic beauty, what could these pictures be used for? They are reminiscent of stars in outer space, and it would be possible to apply image recognition to identify distinct cities and borders such as the 38th parallel across North and South Korea, or the highly populated areas along the Nile.

Figure 1. Division on Korean Peninsula [1]

This is exactly what this research aims to accomplish: autonomous city recognition by shape and size, or proximity to other cities in order to acquire a precise position estimate for Earth orbiting satellites. Furthermore, advancements in multi-camera operations and image processing have been made to the point where real-time stereo vision by a system is attainable. For example, two pictures of New York taken from space could provide an altitude estimate and begin the elaborate process of satellite attitude determination.

In an increasingly congested and contested space environment, traditional sensor failure may become more likely and problematic. Most satellites on orbit are Earth-focused, and small satellites are on the rise in popularity with students and entrepreneurs. A class of high-performing dual-purpose sensors will begin to answer the call for the next wave of innovation.

1.1 Research Questions, Tasks, and Scope

The main purpose of this research is to build upon the work of digital processing cartographers to discover if city lights can be used as a precise method of geolocation and attitude determination. A substantial amount of work has been done on different terrestrial focused sensors over the years in order to obtain the highest caliber of images. Star trackers have been used by some in a dual-purpose manner to retrieve a position estimate. However, this is computationally intensive due to the arduous mathematics already required for a 6 degree of freedom (6DOF) pose, where position is extracted further from that. Most current attitude determination algorithms using visual landmarks are focused on day-time operations and do not function well at night. In order to meaningfully advance the research in this area, sensors must continually strive to be smaller, cost-effective, and computationally efficient. Small satellites (<100 kg) do not always have the capacity for various single-purpose sensors and large

batteries required to run them for every aspect of a mission required for spaceflight. Specific research questions relating to the study objectives are the following:

1. Can a composite of city lights be used in conjunction with daily city lights measurements be used as a database to find position of a satellite in orbit comparable to similar research and with mission-necessary precision?

2. Can a sequence of images taken from space be processed for an attitude estimate of the satellite comparable to a star tracker?

3. Will the functionality of these capabilities compete with that of a Global Positioning System (GPS) and Star Tracker in order to show promise as a viable alternative?

4. Is Open source Computer Vision (OpenCV) an applicable framework for these goals?

5. Can these tools and the assignments be combined to build a Terrestrial Illumination Matching (TIM) algorithm?

1.2 Methodology

The research questions will be addressed by creating a scenario and acquiring a set of images to build a simulation. An algorithm will be developed in two modes that will attempt to accurately determine position and attitude for the system. The scenario will explore different tools and system constraints to identify the best potential methods, and push the boundaries of image processing.

The following assumptions are made:

- Only one satellite and its data will be analyzed.

- The satellite and its camera (and therefore its images) are assumed to be aligned with the orbital frame of the satellite.
- A single pair of image feature detection and feature matching will be employed for simulations.
- The 2 Body Problem (2BP) is used to propagate the satellite's true position in the inertial frame
- In the "Black Marble" composite, discussed later, pixels perfectly correspond to latitude and longitudinal coordinates

1.3 Thesis Overview

Research objectives are outlined in Chapter I and Chapter II reviews relevant research of image recognition and matching with a focus on space-based applications and techniques. In Chapter III, the satellite model is outlined, as well as all coordinate frame transformations from image to the camera to an inertial coordinate. The simulation and algorithm are characterized, and Kalman Filters make their debut to help with any errors the algorithm experiences. Chapter IV will discuss many renditions of the algorithm and its final state, in addition to guiding a discussion to the best methods for each mode of operation, and attempt to show autonomy. Finally, Chapter V summarizes and provides conclusions to the overall research, describes the way forward for further research, and discusses the relevance of the present research.

II. Literature Review

2.1 Chapter Overview

There are a myriad of guidance, navigation, and control (GNC) sensors that are exclusively dependent on the type of vehicle they are aboard, with some techniques described in Table 1. They are created for very specific stages of flight, from hobbyist quadcopters to inter-planetary probes.

Table 1. Aerospace Vehicle Type and Notional Modes of GNC

Vehicle	GNC Methods	Maneuver Method
	AIR	
Weather Balloon	radiosonde, theodolite	pressure inside balloon
Manned Aircraft	altimeter, INS, GPS	thrust, flight control surfaces
Unmanned Aircraft	altimeter, INS, GPS	thrust, flight control surfaces
Quadcopter	visual sensor, GPS	propellor(s)
Airborne Missile	altimeter, INS, GPS	thrust, flight control surfaces
	AEROSPACE	
Scientific Balloon	star camera, altimeter	pressure inside balloon
Sounding Rocket	gyro, altimeter, accelerometers	thrust, flight control surfaces
Space Shuttle	human, star camera	thrust, flight control surfaces
Launch Vehicle	gyro, altimeter, accelerometers	thrust, flight control surfaces
Ballistic Missile	INS, GPS	thrust, flight control surfaces
	SPACE	
Satellite	star, sun, horizon sensor, GPS	thruster, magnetorquer, momentum wheel
Space Station	human, star, sun, horizon sensor, GPS	thruster, magnetorquer, momentum wheel
Interplanetary Vehicle	star, sun sensor	thruster, momentum wheel

This chapter will discuss a few aspects of star trackers and other cameras in space, following their history and exploring their modes of employment. It will also go through the OpenCV library highlighting a few significant algorithms that will be featured in TIM and the process of pose estimation.

2.2 Star Trackers

As shown in Table 1, star measurements and GPS are traditionally used for on-board spacecraft attitude determination and position, respectively, but the use of terrestrial-focused optical sensors for this purpose is growing in popularity. A spacecraft's attitude, also known as its orientation, is used to point the solar panels towards the sun, or to aim communication sensors precisely at their ground stations. First debuted in the 1960s and 70s, star cameras evolved to use a field of stars to include other celestial objects seen through a charge-coupled device (CCD) paired with an extensive star catalogue and a rigorous matching algorithm [3]. In the 1990s there were significant improvements made by the space industry in areas of centroiding accuracy and speed of catalogue matching and computation time. However, star fields, centroiding, and star catalogues form the process that is still mainly used today [4]. Star trackers became very expensive, were known to be heavy, and more innovations to their design were not made until the small satellite revolution. A more recent innovation has been trying to use them not only for attitude determination, but to estimate position of a space-based vehicle as well, where it can be difficult to tell the height above Earth, and requires another computationally intense catalogue search and matrix transformation. One sensor to perform both is desirable for small satellites in terms of space, cost, and redundancy. In 2010, Paluszek et al. successfully used an Unscented Kalman Filter (UKF) with many types of measurements such as range, range-rate, planet chord width, landmark and angle measurements of any

celestial object for deep-space navigation [5]. This, paired with the Inertial Measurement Unit (IMU) allowed for accurate attitude determination algorithms, giving the single star tracker-like sensor a full suite of GNC capability. The system still needed a few different types of sensors, and the employment of a large star catalogue requiring improved matching algorithms or more power and time to be comparable in function to a traditional star tracker.

2.3 Image Processing Algorithms

Star trackers, while being cameras themselves, match to a star catalogue using the geometries of the constellations and brightness, as stars do not provide identifiable features other than slight color variance. Terrestrial images, however, are a different story; filled with colors and interesting land features, they can be be processed using OpenCV, an image processing library in Python that focuses on object recognition, matching, and tracking, mimicing human logic. The definitions that apply to all algorithms in this library to conduct image matching are (1) keypoints, (2) descriptors, (3) matching and (4) outlier rejection. Most algorithms will be explained in a scenario of two images, image A and image B, where image A is analyzed first. A keypoint is the position of a feature of interest in an image. A descriptor is a mathematical way of describing what it looks like. For example, humans have fantastic object recognition for bananas, because that fruit is a curved, yellow, fruit, and they know it is not an apple. Teaching a computer what something looks like can be quite challenging. It is necessary to have keypoint location and description, which make a feature, to employ a matching algorithm. Matching techniques use the location of features and a vector map of their shape and size information to index each set in two images to find matches. Most techniques still do not use color, as standard image processing works in grayscale, and many of these new algorithms have followed suit. Even with a good

set of descriptors, mistakes can be made and outlier rejection techniques are needed to make sure the set of matches average out to the same rotation and translation for an image. If all the matches give different results, it is necessary to throw out outliers to get a usable result. Feature detectors only find a keypoint's position, while a descriptor generator considers its shape. Features can be binary or non-binary, with the former being a vector of bits requiring the Hamming distance to be known in order to conduct matching, while the latter is a vector of numbers that are typically a bit slower and use the L2 norm. The OpenCV algorithms listed below are of special interest, for they implement keypoint recognition and matching between two images.

2.3.1 Both Keypoint Detectors and Descriptor Generators

- SIFT (Scale Invariant Feature Transform): A non-binary algorithm consisting of steps: (1) scale space extrema detection, (2) keypoint localization, (3) orientation determination, and (4) generation of keypoint descriptor [6]. SIFT is unique from other initially discussed image matching algorithms because it is the first to take in the possibility for scaling. Harris corner detection, for example, can only detect corners on a flat plane in an area that keeps the same scale, but can account for some rotation between images. In order to detect corners at various sizes, SIFT uses an approximation of the Laplacian of Gaussian called the Difference of Gaussians (DoG). For each image it gives a scale-space filtering, providing a scaling parameter for each detected feature. DoG produces a list of scaling parameters found by blurring the image and comparing with surrounding pixels to find the best scaling parameter for each keypoint, then is saved with the keypoints position for each image. A Taylor series expansion of scale space is used to get a better coordinate of a keypoints position and to conduct rejection of certain keypoints if the intensity of the extrema is less

than a set threshold value. This prevents edges and low-contrast keypoints from being saved, keeping only strong keypoints that are not as general to images. Orientation is determined by creating a histogram of the pixel neighborhood around the keypoint location plus scale information and then using the highest peak and any peak above 80%, which contributes to accurate matching. The histogram of the neighborhood is cut into four quadrants and represented as a vector to create a keypoint descriptor and sized according to scale information. Keypoint matching is conducted by finding nearest neighbors of location and descriptor. The nearest neighbor is defined as the keypoint with the minimum Euclidean distance for the descriptor vector [6]. False matches are avoided by conducting Lowe's Ratio test of the distance to a keypoint's nearest and second nearest neighbor, setting the ratio to be greater than 0.8.

- SURF (Speeded Up Robust Features): Another non-binary algorithm that filters at a larger scale, finds orientation from Haar-wavelet responses, and uses rectangle windows to align images [7]. It is best described as a faster version of SIFT. Instead of using the Laplacian of Gaussian, which is computationally expensive, it instead uses the Box Filter. The algorithm blurs pixels and assigns values to the blurred blocks, then uses the determinant of the Hessian matrix for scale and location of a keypoint. For orientation, SURF uses Haar-wavelet responses in a neighborhood with Gaussian weights applied and then averages them. The wavelet responses are used again for feature description, cut into quadrants (similar to SIFT), and a vector is formed from the sum of the lengths of the wavelets in each quadrant. It is three times faster than initial corner and feature detectors, capable handling images with blurring and rotation, and creates more keypoints, but is not as effective for viewpoint or illumination changes [7].

- BRISK (Binary Robust Invariant Scalable Keypoints): Born from SIFT, BRISK also implements elements of FAST's arc pixel detector, able to set thresholds and number of pixels searched along an arc. Combined with SIFT, FAST's nonmaximal suppression can be applied across the scale space [8]. This means a feature is kept when it is either a maximum or minimum within its scale, but also across scale space. Descriptors are found by applying Gaussian smoothing and calculating gradients between points. The average gradient is calculated and an intensity value is rotated by the gradient direction to make the descriptor rotation invariant [8].

- ORB (Oriented FAST and Rotated BRIEF): This algorithm combines FAST as its feature detector and BRIEF as its descriptor generator to fix shortfalls found in both. FAST is used to apply a scale pyramid rather than just using the original image and is oriented by assuming the intensity centroid would be offset from the center of a detected corner [9]. Descriptor generation is similar to O-BRIEF, but the pixels are rotated by orientation of the feature before the random Gaussian gradient is taken to compute the descriptor. The best matches are based on which has the greatest variance and mean of 0.5 [9].

2.3.2 Keypoint Detectors

- FAST (Features from Accelerated Segment Test): FAST is built from corner detectors, and operates by looking at a circle of pixels around a potential feature and their intensity values [10]. When the intensity varies around a certain arc, the corner of a feature can be detected and that is saved as the keypoint. It can be optimized by setting different thresholds of pixel intensity to look at, and only certain pixels around the arc, rather than every single one. A feature and keypoint is saved when the sum of absolute difference between the point and

its surrounding pixel values are the strongest for the image, called nonmaximal suppression, which can be set as the algorithm is employed.

- MSER (Maximally Stable Extremal Regions): This algorithm is different from most others where it does not particularly detect keypoints in areas of interest, but rather hulls or blobs [11]. These hulled areas have distinct shapes that can then be centroided to a keypoint and used with the following algorithms. MSER operates by creating a binary image based on a certain threshold of pixel value, and identifying contiguous regions within that image [11]. A sequence of images is created from the original by varying the threshold, and the regions that are constant across a range are saved as hulls. This is good for identifying specific shapes and areas of contrast, which could prove to be lucrative in a blob-search and match of city lights experiencing saturation of pixels.

2.3.3 Descriptor Generators

- BRIEF (Binary Robust Independent Elementary Features): Created out of a desire to have a binary descriptor that would be faster to compute and compare features than non-binary descriptors. BRIEF operates by testing pixel intensity of smoothed versions of patches near a keypoint [12]. A random Gaussian distribution of a bitstring across a patch gave the best results for uniqueness in order to match descriptors. However, it was not rotation invariant like some other descriptor generators, which led to Oriented-BRIEF (O-BRIEF) and later ORB.

- FREAK (Fast Retina Keypoint): FREAK is one of the most interesting algorithms, inspired by the design of the retina, taken from how the number of ganglion cells varies around the eye and are most dense around the fovea [13]. This means there are bigger areas and descriptors computed around the outside

of the image, and smaller, more unique ones around the center of the image. Similar to ORB, different pairs of points were tested to compare before finding conditions for the best points to compare for accurate matching. FREAK also applied Saccadic Search", meaning that a preliminary match is found using the first 16 matches, followed by a rigorous re-matching to find the best out of those [13]. Despite being more creative and using different approaches, it is considerably faster than the most common algorithms (SIFT, SURF, and BRISK), but not necessarily more accurate.

2.3.4 Feature Matching

- Brute-Force: the L2 norm is used to calculate distance between two matches, and selects the feature in image B that has the smallest distance [14]. It is the simplest way to match features. The matcher compares each descriptor in image A and finds the closest match in image B and, when using knnMatch, will only draw a number, k, of the best matches to be used. The user can set that they only need 10 matches, for example, and it will pull the ten best matches.

- FLANN (Fast Library for Approximate Nearest Neighbors): Features from image A build a kd-tree (a data-structure enabling much faster search for a descriptor), and features from image B are matched, well-suited for large image databases and smaller images to match [15]. A kd-tree is a nearest-neighbor search that goes to the k-th dimension. Once FLANN finds a potential keypoint, it creates branches until it finds nearest-neighbor keypoints, and can go to any k dimension to span a part of the image (higher dimension takes longer but could span the whole image). The shape of these trees are the feature keypoints and descriptors, and similar kd-trees are compared in shape in order to find matches. FLANN allows the user to set targets for precision, such as 20%

probability nearest-neighbor matches return an exact match. Higher values take longer, but are more accurate.

2.3.5 Outlier Rejection

- Lowe's Ratio Test: Once a complete set of usable matches are made for each set of images, before displaying the images and saving the data, those matches are determined good or bad with Lowe's test, which throws out matches that do not follow the average slope of all the lines created described by:

$$\mathrm{D}(\hat{\mathbf{x}}) = \mathrm{D} + \frac{1}{2}\frac{\partial \mathrm{D}^{\mathrm{T}}}{\partial \mathbf{x}}\hat{\mathbf{x}} \tag{2.1}$$

  where D is the distance between a matches nearest-neighbor [6]. This ensures that only the best matches are used, which in turn gives the most accurate assessment of the pose matrix.

- RANSAC (RANdom SAmple Consensus): Randomly selects a minimum number of points required to fit a line of data and tries to fit the model and reject outliers, repeats this until inliers are maximized, ensuring good matches [16]. RANSAC is a filter that can be applied while Brute-Force matching is taking place that applies geometric constraints to the matching technique.

2.3.6 Pose Estimation

The pose of a camera at a point in time is described as a 4x4 matrix comprised of the relative change in attitude and the relative change in position from the camera's initial position. The relative pose between these images is found using a recovering process, from either an Essential or Fundamental matrix, following Scaramuzza's work [17]. These matrices describe position of a matched object in two images while

satisfying the Epipolar constraint, a line between two cameras, that mathematically describes if an object is found in both images, there is a certain plane both the cameras must lie on [17]. The equation for the Epipolar constraint is defined as:

$$\underline{\mathbf{x}}_{\mathrm{n}_1}^{\mathrm{T}}(\mathbf{t} \times \mathbf{R}\underline{\mathbf{x}}_{\mathrm{n}_0}^{\mathrm{T}}) = 0 \tag{2.2}$$

where $\mathbf{x}$ is the position of the object in normalized coordinates in each image, $\mathbf{t}$ is the translation between the two cameras, and $\mathbf{R}$ is the rotation between the cameras [17]. The Epipolar constraint is rewritten as the following linear equation:

$$\underline{\mathbf{x}}_{\mathrm{n}_1}^{\mathrm{T}}[\mathbf{t}_{\mathrm{x}}]\mathbf{R}\underline{\mathbf{x}}_{\mathrm{n}_0}^{\mathrm{T}} = 0 \tag{2.3}$$

where

$$[\mathbf{t}]_{\mathrm{x}} = \begin{bmatrix} 0 & -\mathrm{t_z} & \mathrm{t_y} \\ \mathrm{t_z} & 0 & -\mathrm{t_x} \\ -\mathrm{t_y} & \mathrm{t_x} & 0 \end{bmatrix} \tag{2.4}$$

.

The matrix $[\mathbf{t}]_{\mathrm{x}}$ is redefined using the Essential Matrix, E:

$$\underline{\mathbf{x}}_{\mathrm{n}_1}^{\mathrm{T}}\mathrm{E}\underline{\mathbf{x}}_{\mathrm{n}_0} = 0 \tag{2.5}$$

where

$$\mathbf{E} = \mathbf{R}[\mathbf{t}]_{\mathrm{x}} \tag{2.6}$$

and the Essential Matrix can be scaled or unscaled. If scaled, then the scale is known from the two images, and reflects six degrees of freedom. Other constraints on the Essential Matrix that help solve for E are the following:

$$\det(\mathbf{E}) = 0 \tag{2.7}$$

$$2\mathbf{E}\mathbf{E}^{\mathrm{T}}\mathbf{E} - \mathrm{trace}(\mathbf{E}\mathbf{E}^{\mathrm{T}})\mathbf{E} = 0 \tag{2.8}$$

.

The Fundamental matrix follows the same process, but with feature locations in the images in pixel coordinates, rather than normalized. The pose is then recovered from the Essential or Fundamental matrix. A pose matrix is a 4x4 matrix comprised of a 3x3 ortho-normal rotation matrix, $\mathbf{R}$, which can be rotated to a body to orbital attitude, and a 3x1 translation vector, $\mathbf{t}$, in ECI coordinates. It is typically represented as

$$\mathbf{T} = [\mathbf{R}|\mathbf{t}] \tag{2.9}$$

and expanded as

$$\mathbf{T} = \begin{bmatrix} \mathrm{R}_{11} & \mathrm{R}_{12} & \mathrm{R}_{13} & \mathrm{x} \\ \mathrm{R}_{21} & \mathrm{R}_{22} & \mathrm{R}_{23} & \mathrm{y} \\ \mathrm{R}_{31} & \mathrm{R}_{32} & \mathrm{R}_{33} & \mathrm{z} \\ 0 & 0 & 0 & 1 \end{bmatrix} \tag{2.10}$$

put homography in if you fix your other eq'ns

A mix of different algorithms must be used to get a full, accurate result. The first step is feature recognition, and SIFT and SURF conduct both feature recognition and descriptor generation, so specific qualities of the image can be matched. Brute-Force and FLANN are chosen for matching, allowing different uses of the descriptors and thresholding applied. FLANN is more difficult to implement but yields better

results since Brute-Force is simple, larger rotations or translations of the satellite could render it useless. Finally, RANSAC conducts outlier rejection, ensuring the best measurement possible from the image is chosen. That set of points is then used to create the Essential or Fundamental matrix using Equations 2.7 and 2.8. Remembering that E describes the rotation and translation, the Pose, T, can be recovered from that and put in the form shown in Equation 2.9, where it can be used further for navigation. On a terrestrial level, Veth and Raquet have contributed many works on passive navigation methods using these OpenCV techniques that are widely cited [18, 19].

2.4 Defense Meteorological Satellite Program

Since the 1970s and with the debut of the U.S. Air Forces (USAF) Defense Meteorological Satellite Program (DMSP), space sensors have been able to detect the visible spectrum and more, allowing the Earth to be seen in a whole new way [20]. The main priority of scientists using this new data was to create high precision maps of the world, which involved heavy data processing and proved very difficult as only film strips were available for decades. Over the 1990s and until now, Elvidge and many of his collaborators have dominated precise geolocation of data from DMSP's Operational Linescan System (OLS), designed specifically to sense low levels of visible and near-infrared (VNIR) radiance during nighttime operations [20].The goal of the work was to separate constant light emissions from urban areas, such as cities, towns, and industrial sites, from noise and outliers like fires and illuminated clouds. OLS is an oscillating scan radiometer with a swath of 3000 km and, aboard DMSP, acheives global coverage of the earth four times a day, during Civil Twilight events and between them [20]. Evening Civil Twilight is defined as the period that begins at sunset and ends in the evening when the center of the sun's disk is six degrees below

the horizon and morning Civil Twilight is the equivalent that starts before sunrise and ends at sunrise, and will be measured with solar elevation angles [21]. Night is hereafter defined as the period including and between Evening Civil Twilight and Morning Civil Twilight.

Using 236 smooth revolutions of OLS, pixel data is collected and screened for city lights during night in each dataset, where each kilometer of earth in a pixel is given a percentage of city light occurrence [20]. This method of map making found occurrence of night-time lights from large cities that were at least 10% cloud-free at least 99% of the time, but did not result in a composite image of the Earth that year [20]. The largest improvement of using DMSP OLS data to create a composite came in 2009 from Elvidge's colleague, Baugh, who created a Stable Lights product that heightened geolocation accuracy, included smaller city detection to a greater degree, and managed incorporation of data from higher latitudes [22]. Baugh accomplished this by implementing a system of thresholding, assigning pixels a Digital Number (DN) threshold for day, nighttime marginal, zero lunar illuminance, clouds present, and no data [22]. The Stable Lights product used suborbits flagged with zero lunar illuminance, which were then reprojected on a 30-arc second grid where overlap of areas covered, noise, and higher latitudes were excluded. The suborbits can then be further processed and lined up for a composite by identifying land-sea boundaries and conducting outlier rejection of anomalies like fires. The work resulted in composites of the Earth for the entire digital archive of OLS data from 1992 to 2009, which allowed researchers to use this for further scientific study [22].

2.5 Suomi National Polar-orbiting Partnership

Suomi National Polar-orbiting Partnership (NPP) was the result of a National Oceanic and Atmospheric Administration (NOAA) and Natinal Air and Space Agency

(NASA) collaboration as a multi-purpose stop-gap in support of the expansive Earth Observing System (EOS) collection of satellites. The NASA EOS family, which includes satellites like the LANDSAT series, has a very generous open source and sharing community, having created many online tools for viewing data. Suomi NPP was launched to an altitude of 824 kilometers in a 98.7° sun-synchronous near-polar orbit with a 101-minute period and a Descending Node at 10:30 hours [23]. The satellite commenced operations in 2012, Suomi NPP is able to see the entirety of the Earth twice a day (entire Earth during night and day), and has a 16 day cycle for careful juxtaposition of data over time. Two-Line Element (TLE) sets that describe a satellite's precise orbit at a certain time, provided by North American Aerospace Defense Command (NORAD), are readily available for this system on space-track.org [24].

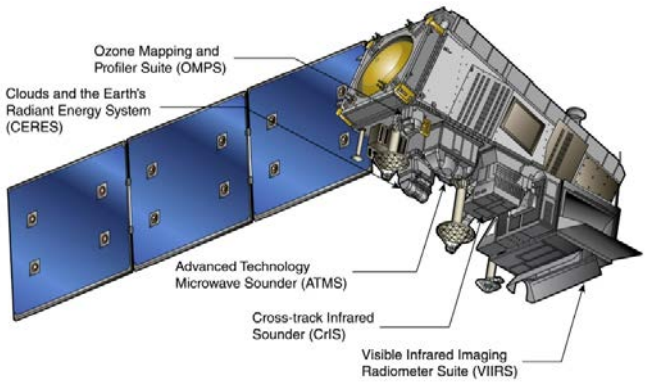

Figure 2. Suomi National Polar-orbiting Partnership (Image credit: NASA/NOAA)

The sensor on Suomi NPP that provides terrestrial imagery for this project's data collection is the Visible Infrared Imaging Radiometer Suite (VIIRS). VIIRS is located on the nadir-pointing end of the spacecraft, slightly offset from the body axes as shown in Figure 2. While VIIRS has 22 channel range of light collection bands, only the Day/Night Band (DNB) is used for this work, as its purpose is specifically to gather artificial city light at night. VIIRS uses a whiskbroom scanning method that is able to take a swath of 3000 km at once allowing for global nighttime coverage every day

[25]. It is specifically designed to control pixel size and prevent aggregation using a bow-tie deletion scheme (since Suomi NPP is in a polar orbit) tracking scan overlap and pixel location in the track direction. DNB is centered at 0.7 microns in the visible spectrum, but with a very wide forward width at half maximum (FWHM) of 0.4 [25]. This allows for all light from the Earth to be picked up by the sensor in a way that is high-contrast and impedes the effects of albedo light. Data from this satellite, and specifically DNB, is available daily on NASA's EOS Data and Information System (EOSDIS) using the Worldview tool [26]. Worldview allows the user to see data collected by DNB the same day it was collected, and look historically to 2017, as well as to "Black Marble" composites from 2012 and 2016. Black Marble is created using clear data throughout the year from DNB, building upon Baugh's work using DMSP OLI data of city lights around the world to create a cloud-free composite image with stunning resolution [27].

Figure 3. NASA's Black Marble (2016)

The composite of the year, shown in Figure 3, can ensure a cloud-free pixel for every corner of the Earth, but looking at a composite of the day in Figure 4, this is not

the case. During summer months in certain parts of the world, a monthly composite is not even possible due to excessive atmospheric light, rendering observations useless [28]. The varying levels of processing able to be accessed of VIIRS data, raw from the satellite to a yearly perfect composite, is impelling curiosity across all disciplines.

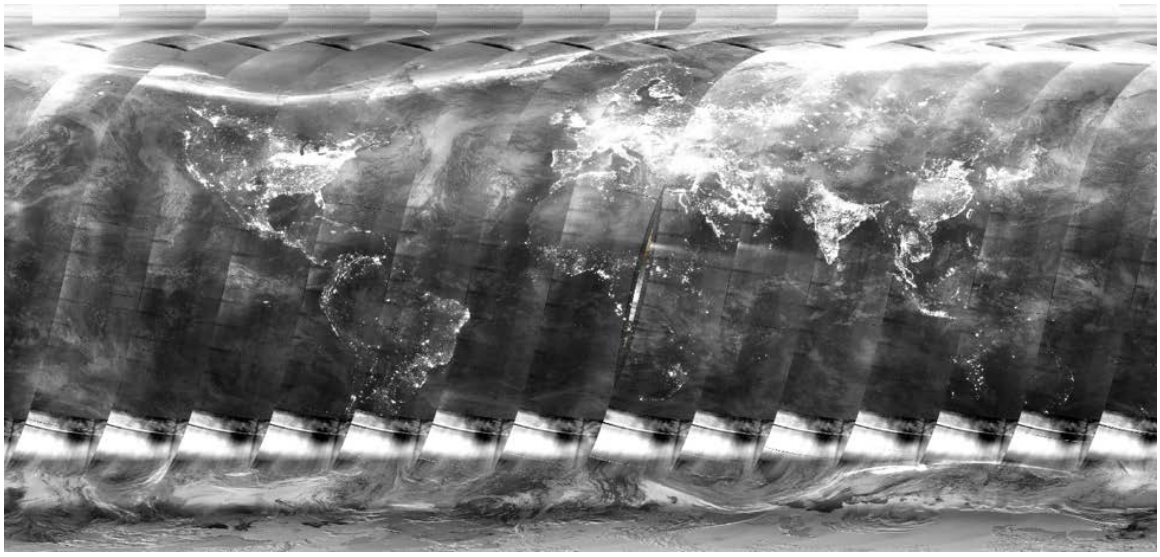

Figure 4. EOSDIS Data Pull from Summer 2019

2.6 Cartography and its Services

City lights data from DMSP OLI and Suomoi NPP VIIRS have been used for various disciplines and forms of analysis from cartography to the estimation of Gross Domestic Product (GDP). Imhoff et al. applied thresholding techniques at 89% frequency to be considered an urban pixel to the United States to compare population and housing density to 1990 US Census data with wildly varying results state-to-state [29]. An example of this used in a less developed area was done by Amaral et. al., who used DMSP night-time city lights to estimate the size of settlements in the Brazilian Amazon Rainforest [30]. The goal of this work was to understand how best to support sustainable development in urban and rural areas as they experience

human population growth. The DMSP imagery was paired with reliable census data from the region.

Cloud-cover and pixel saturation posed huge problems to actually using this data, and that was solved by NOAA/National Geophysical Data Center (NGDC) and used in Elvidge et al. 1997b. Amaral first had to use DMSP data collected from a period from January to June 2002 to create a cloud-free mosaic. This was accomplished by taking the collection of images from that time and assigning each pixel a Digital Number (DN) that corresponded to the amount of light and cloud cover. The mosaic was created from cloud-free and lighted pixels. The city-lights result from the mosaic was compared with census data and in-person field expeditions to small villages. Amaral was successfully able to identify cities with more than 20,000 people 100% of the time, 95% for populations between 10,000 and 20,000 people, 82% for 5,000 to 10,000 people, and only 35% for populations less than 5,000 people [30]. Mapping settlements with less than 2.5km^2 well-lit area was not feasible with DMSP data. Improved remote-sensing capabilities were called upon by many communities, and were answered with Suomi NPP VIIRS.

Elvidge in 2013 took the lead on comparing the two sensors, looking at footprint, Earth coverage, quantization,low-light collecting ability and pixel saturation. Data collected from VIIRS is 45 times more fine and has a constant 742 m x 742 m pixel footprint, compared to DMSP OLS 5 km x 5 km footprint that experiences pixel expansion towards the edges [2]. This allows for considerably more precise map-making and analysis of the urban areas by VIIRS. Elvidge verified these upgrades mattered by creating a composite of each sensor's nighttime lights using only two months of data shown in Figure 5 of Oahu, Hawaii, where the precise sprawl of the population can be seen distributed on the coast, and a little bit in the center of the

island, whereas OLS on the right leads the viewer to believe the spread of people along the coast is a lot more dense than it really is [2].

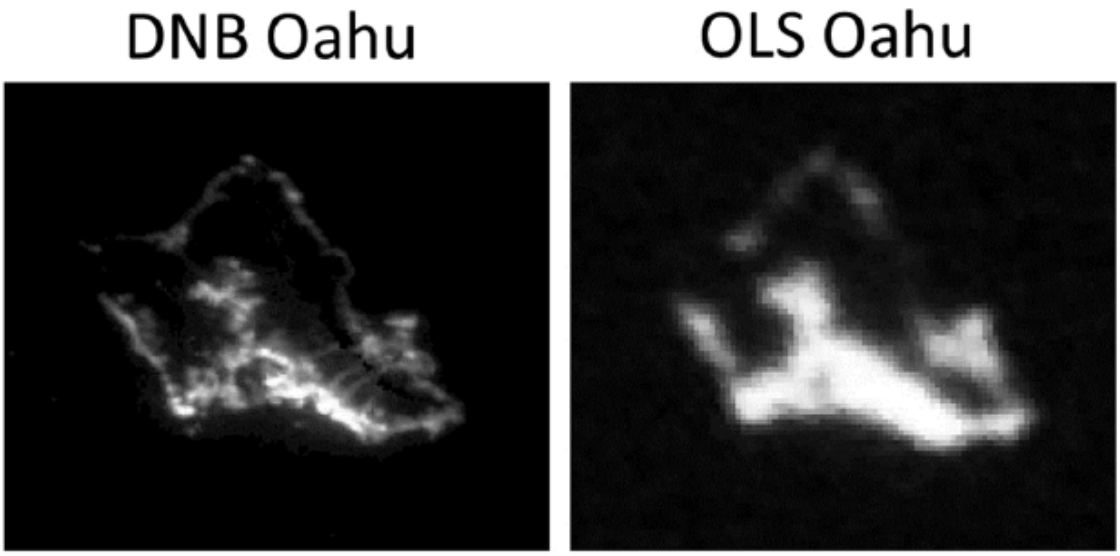

Figure 5. DNB vs OLS exact light locations [2]

This revelation prompted similar works to Amaral's, with Checa et al. using DNB data to measure the urbanization of the Iberian Mediterranean Coast [28]. Instead of only looking at population, Checa attempted to categorize the socio-economic status of microregions within the Iberian Coast by looking at the intensity of city lights. Using NOAA's published monthly composites, Checa further processed the cropped target area for anomalies such as fires and clouds, using a threshold of a pixel's average value. Checa concluded the level of detail the composites provided made it possible to study the intensity and seasonality of urban areas, looking at how land is used and whether that matches with the population expected, a much more decisive conclusion than of Amaral's use of DMSP OLS data [28]. Considering a sensor can tell the precise energy use of a neighborhood in Spain, surely it could be used for precise satellite pointing.

In 2011, just as Suomi NPP was preparing for launch, Klancar developed an attitude control algorithm that was tested in simulation using Simplified General Perurbations 3 (SGP3), Google Earth, and SIFT [31]. The attitude dynamics and kinematics were propagated, with reaction wheels as the control system. Klancar simulated the orbit of Lapan Tubsat at 600 km above Earth with an orbital period of 90 minutes by using a sequence of Google Earth images as Earth observations at 10 Hz sampling frequency [31]. The camera resolution was set at 320 x 280 pixels, giving a 2.5 meter per pixel resolution, that they down-sampled to 15 meters per pixel to simulate what a camera could see from LEO [31]. The sequence of images was created for the exact SGP3 position, as well as for the 2BP, and the sequences were compared image by image to initiate the control law. The difference in pose of the images was calculated by using SIFT and Lowe's ratio test, set at 0.6 [31]. A comparison of the pose and estimated Euler angles were used to calculate the appropriate moments for the reaction wheels. The performance of this simulation showed that it was comparable to a star tracker and much better than the expected accuracy of a sun sensor [31].

Similarly in 2015, Straub used MATLAB's Global Self-Consistent Hierarchical High-Resolution Geography (GSHHS) to simulate terrestrial images, and then use coastline data to match and obtain a position estimate [32]. The fictional satellite was assumed to be in a 1,000-km altitude orbit with a 56° and a 30° field of view (FOV). These were chosen to maximize the visibility of coastlines, with images taken every five minutes, and the errors at different inclinations were analyzed. After many terrestrial images were simulated and matched for several geographically separated locations, an extended Kalman Filter (EKF) was applied to produce actionable estimates.

Kouyama used observations from UNIFORM-1, SURF, and RANSAC to identify landmarks for attitude determination. Baseline images for the locations studied were

taken from Landsat-8's Operational Land Imager (OLI) and position was propagated from a TLE [33]. A slightly different perspective was recorded of the UNIFORM-1 and OLI images and compared using OpenCV techniques. The same time step of images were compared to each other, and the pose estimated; assuming the OLI images were aligned with the boresight, the attitude of UNIFORM-?1 could be recovered from the pose. This was completed and attitude determined with an accuracy of 0.02°, comparable to star trackers [33].

2.7 Summary

This chapter showcased historical and contemporary research of a new age of space-based cartography and its suppliers, image processing algorithms and their navigation techniques. OpenCV is a popular choice for visual navigation applications, especially for the post processing of satellite imagery, and is becoming more popular for imagery tools onboard small satellites after real time video capability on a smartphone was attained. It is especially fantastic because in order to attain operational tracking accuracy, camera calibration is not necessary. The current research seeks to develop a methodology to conduct spacecraft positioning and attitude determination using terrestrial lights as a surrogate for star fields, and provide an alternative means of pose estimation in the event of star sensor malfunction using the OpenCV framework.

III. Methodology

> "It is this love of the contemplation of the eternal and unchanging which we constantly strive to increase, by studying those parts of these sciences which have already been mastered by those who approached them in a genuine spirit of enquiry, and by ourselves attempting to contribute as much advancement as has been made possible by the additional time between those people and ourselves."
>
> - *Claudius Ptolemy, Almagest*

3.1 Initial Assumptions

The current research proposes an algorithm that will take snapshots of image data from VIIRS DNB with a set FOV and use them in sequence and compared to Black Marble for pose estimation. Each image in succession will go through Terrestrial Illumination Matching (TIM) technique using OpenCV and MATLAB created images of the spacecraft's ground track over the most recent rendition of Black Marble (2016). Two modes of TIM may be employed: (1) position determination; and (2) pose and attitude determination. Position determination operates by matching real data, such as images from Worldview, to Black Marble by identifying precise latitude and longitude coordinates of cities. Attitude determination will assume initial orientation and inertial position is known, and use OpenCV for pose estimation, obtaining attitude change in each image and relative motion from the last position update. A pose matrix is a 4x4 matrix comprised of a 3x3 ortho-normal rotation matrix, $\mathbf{R}$, which can be rotated to a body to orbital attitude, and a 3x1 translation vector, $\mathbf{t}$. Other than pose between images, there is a intricate relationship of spacecraft position around a rotating Earth. It is essential to the work to have accurate rotation matrices through all the coordinate frames, and to properly propagate the satellite motion over time.

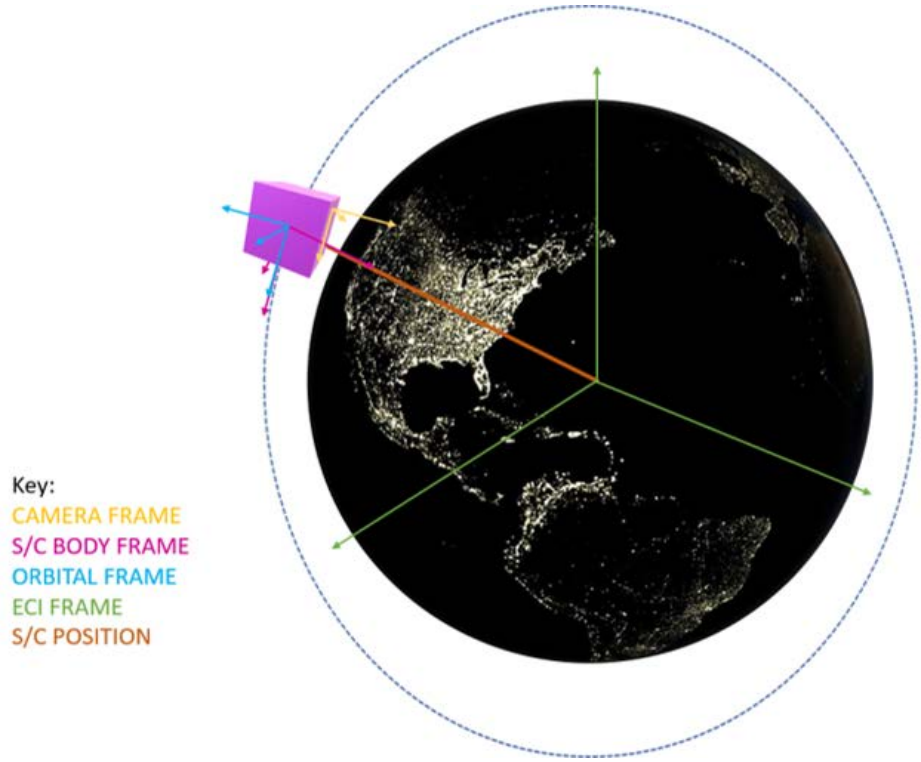

Figure 6. Simplified model of Suomi NPP around Earth at Night

The inertial coordinate frame used in this work will be the Earth Centered Inertial (ECI) coordinate system, a geocentric equatorial system typically described by "IJK" where the fundamental plane is the Earth's equator, the I axis points towards the vernal equinox, the J axis is 90° to the east completing the right-handed system with K through the North Pole [34]. The orbital frame is described as Radial, In-track, Cross-track (RIC) and shown as o in Figure 7, but Euler Angles are used to describe equivalent axis with RIC correlating to pitch, roll, and yaw [34]. The spacecraft body frame is assumed to be aligned with the orbital frame and DNB's camera frame. These frames and their relationships can be seen in Figures 6 and 7 more closely. Looking to the Earth, the coordinate system fixed to a rotating Earth will be Earth Centered Earth Fixed (ECEF) where the system follows the same fundamental plane as ECI, the X axis points to the intersection of the Prime Meridian and the equator,

the Z axis points through the North Pole, and the Y axis completes the right-handed system.

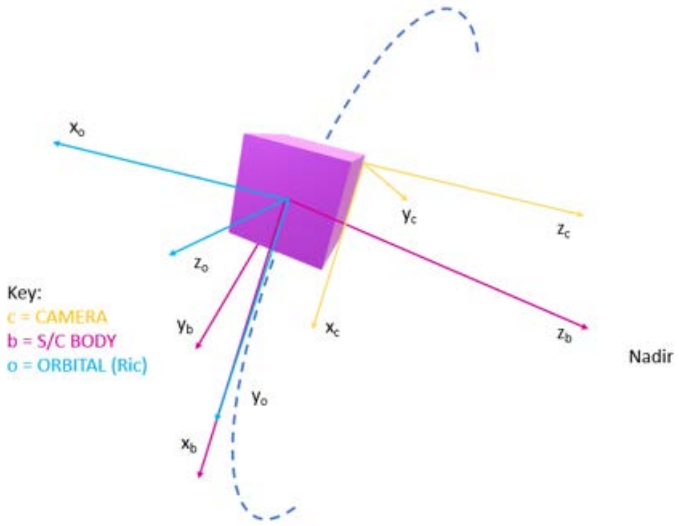

Figure 7. Close up of coordinate frames

The following sections will detail how a simulated model of the spacecraft's motion and the images it sees were created, how images were collected from Black Marble and Worldview and matched, and how the algorithm can be further employed with a Kalman Filter.

3.2 Simulated Model

A simulated model was needed in order to match the timing of image collection with the spacecrafts position. Two TLEs were chosen from the past year of Suomi NPP's orbit and were chosen by looking through Worldview for days that had complete data acquisition and clear skies around the world. The most common area analyzed, including in early versions of this work, contains the Great Lakes and Midwest region of the United States, shown later in Figure 10. The Veteran dataset, taken on 11 November 2018 (Veteran's Day), has a short pass over the center of the United

States. The Woman dataset, taken 8 March 2019 (International Womens Day), has a short pass over Eastern Russia down to Sri Lanka, which includes the possibility of using coastlines of the Bay of Bengal and city lights in conjunction for position determination, building off of Straub's work [32]. Both have a short nighttime pass that just tests 50 minutes of orbit determination, and are run for 24 hours with full world coverage as well. The intertial position, velocity, and time from the TLEs are then propagated to get a simulation of the orbit track for the entire day, which can be matched up to the available swaths on Worldview. The 2BP

$$\ddot{\mathbf{r}} = \frac{-\mu}{r^3}\mathbf{r} \tag{3.1}$$

where $\mathbf{r}$ is the spacecraft's inertial position, and $\ddot{\mathbf{r}}$ is inertial acceleration, was propagated in time using a six-stage, fifth-order, Runge-Kutta numerical integration method. This data can then be plotted on a three-dimensional globe, to show the full orbit tested, shown in Figure 8.

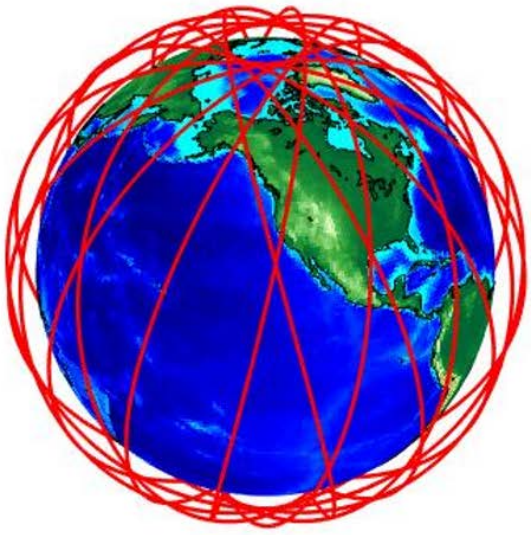

Figure 8. Veteran's Day TLE propagated for 24 hours

The Julian Day from the TLE's epoch was used to convert all ECI coordinates through ECEF into Llh so the ground track of the satellite can be shown on a two dimensional map. Black Marble is a flat image, with a resolution of 13500 x 6750 pixels of equal size. Each pixel coordinate can also be converted to latitude and longitude, knowing the image spans exactly the Earth's dimensions 180° latitude and 360° longitude. This would not be true at the poles, however since there are not usable city lights data over the poles, this is ignored for now. From here, the spacecrafts orbital ground track and VIIRS FOV ground track are shown in Figure 9. The FOV for the simulation was chosen to have a resolution of 3000 km, DNB's full resolution, which was plotted in Figure 9.

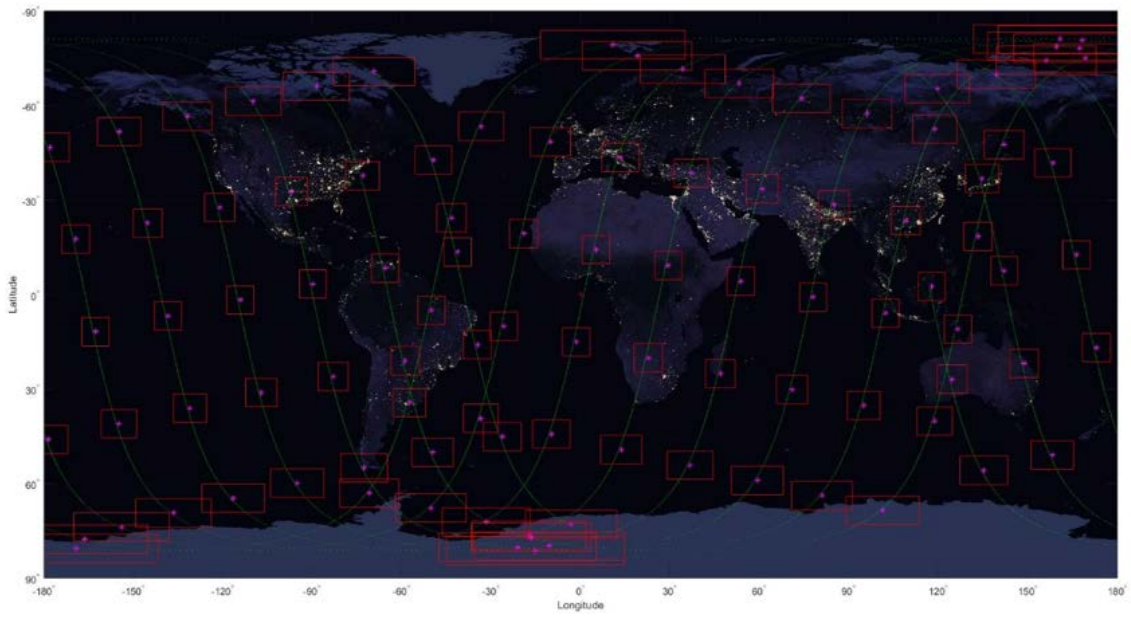

Figure 9. Black Marble with Suomi NPP and VIIRS Ground Track

Applying this method to the chosen TLEs, specifying propagation direction of time (due to time of day the TLE comes in, moring or late at night) and the amount of time the spacecraft should travel before it collects another image, gives the Veteran and Woman image sets. This information is outlined in Table 2.

Table 2. Dataset Names and User Input

Data	Propagation	Location	Sim Time (s)	# of Images
Veteran	Backwards	SE Asia	3000	1
		Arab Gulf	4500	1
		Great Lakes	6000	1
		USA	6000	5
Woman	Forward	Italy	1000	1
		India	8000	1
		EU	500	6

The simulated images are created from Black Marble and from Worldview with the same FOV, shown in Figures 10 and 11. Each red FOV box is then saved in a specified folder as its own image, with no markings or borders from MATLAB and the pixel resolution is downsampled to provide noise in the data. These individual images are shown on the side of each figure, in the same progression as they were taken. The reason for saving the individual images is to be read-in to Python where TIM is built with OpenCV, which will be discussed in the next section. All borders and location identifiers must be removed because it could trick the image matching algorithm into matching features that are not just city lights. The difference between how well Black Marble removed impurities to make the composite is easily seen when comparing Figures 10 and 11. The ability to pull pictures from Worldview is unique to this work and essential for a real-world algorithm due to its natural noise. This concludes the image acquisition process, and now the image matching techniques can be tested.

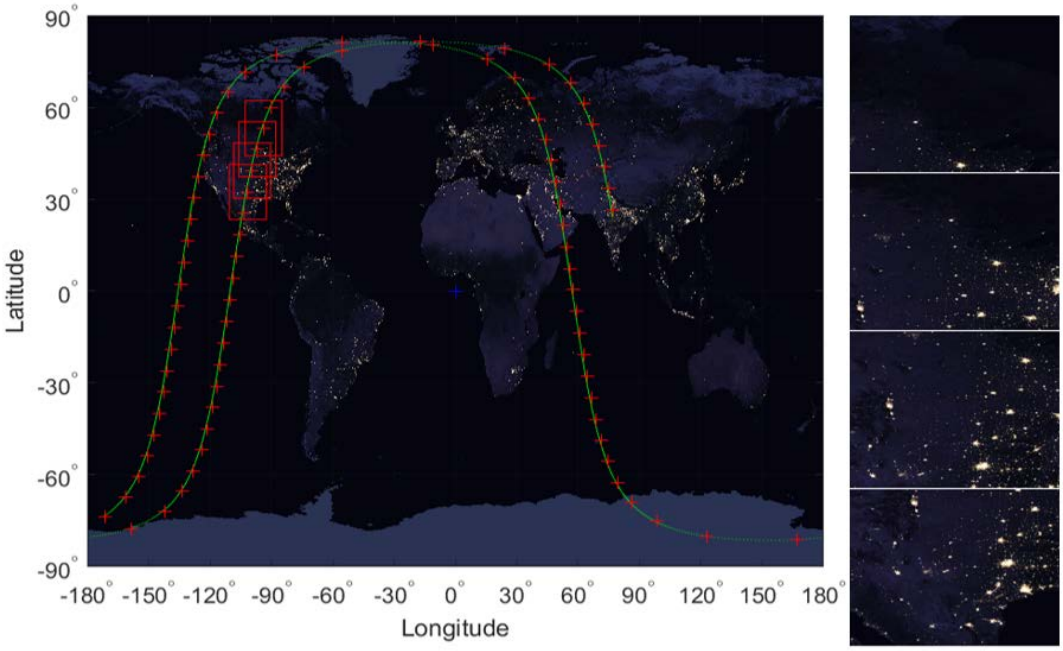

Figure 10. Veteran, Great Lakes on Black Marble

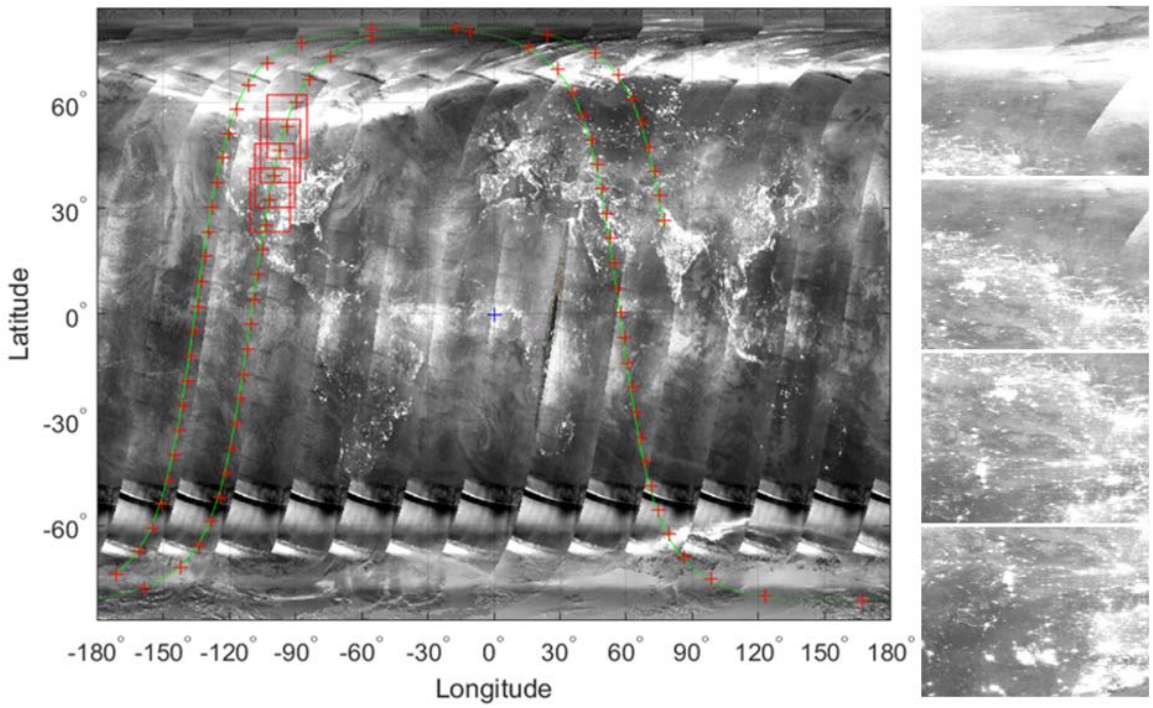

Figure 11. Veteran, Great Lakes on Measurement Image

3.3 Image Matching

Once two images are collected, TIM can be employed via the process outlined in Figure 12. The two images are compared using some of the OpenCV techniques described in section 2.3, giving Euler angles and relative position change from image A to image B. Both sets of data have more than two images, and they are processed in a loop where image A and B are compared, and then image B becomes image A, and is compared to a new, third image, which becomes image B. There is the option to compare the third image to the first image, but that must assume the FOV of the first and third image overlap to some degree, requiring shorter time between images taken. An optimization of step size and number of features required for accurate detection is planned for the future. Once all images are compared and pose found for each image relative to the first, the position data is able to be run through a filter. The filter's purpose is to enable the ongoing determination of position in the case of a bad measurement or over large bodies of water.

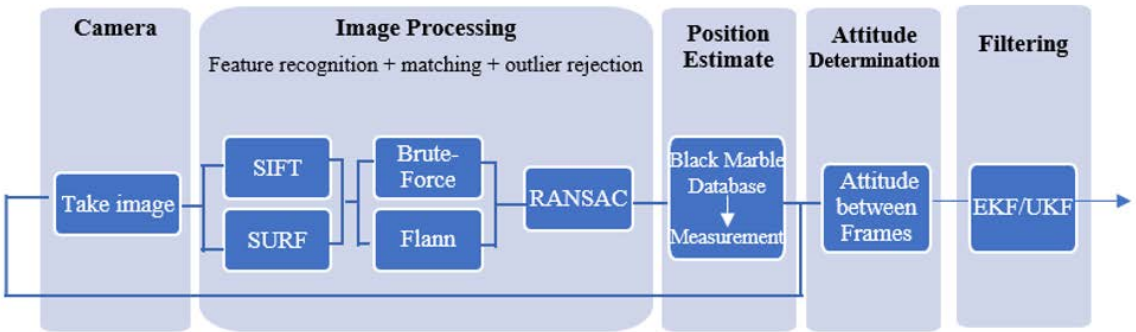

Figure 12. TIM Flowchart

SIFT and SURF were chosen due to their high likelihood of success finding good matches in the images relatively quickly, meaning there are more matches to go through Lowe's test and outlier rejection. To verify this, thirteen combinations of

common OpenCV algorithms involving feature detection, descriptor generation, and matching were tested. Mode 1 entails matching the first image to Black Marble, to find its true position, an example shown in Figure 13. Black Marble acts as a database, in the same way a star catalog does for a star tracker.

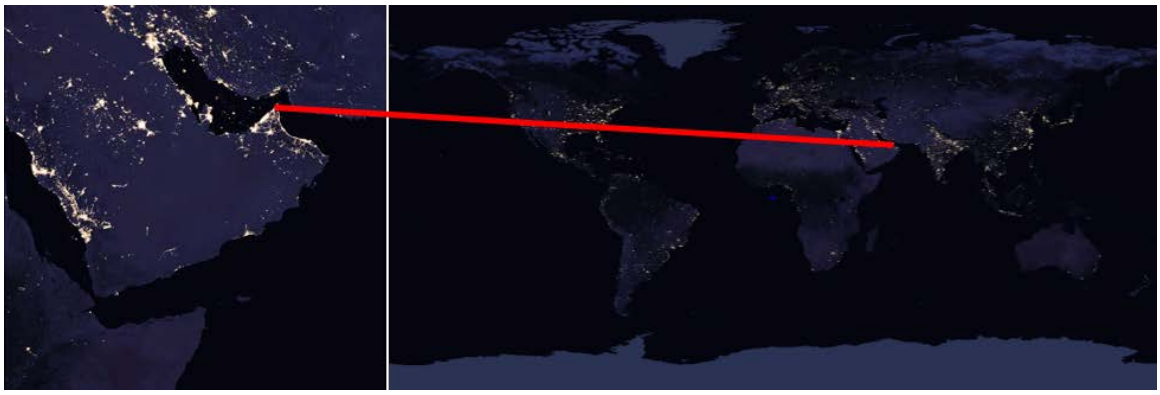

Figure 13. Mode 1: Comparing New Image to Black Marble, finding Jebel al Harim, Oman

The following work in relative position change and attitude determination, Mode 2 of TIM, uses SIFT, and is initialized to begin image processing. The image is read in and converted to grayscale for analysis, then SIFT finds keypoints and descriptors in that image. A loop is created to cycle through any number of successive images, but in this, simple case, there is only one further image. The image is read in and a second set of keypoints and descriptors are determined. FLANN uses the descriptors to find matches in shape, size, and intensity. In order to be considered a match, Lowe's ratio test is applied, described in Equation 2.1 [6]. Figure 14 shows New Orleans (a descriptor) matched between two images, and the line drawn between it after determined to be a good match.

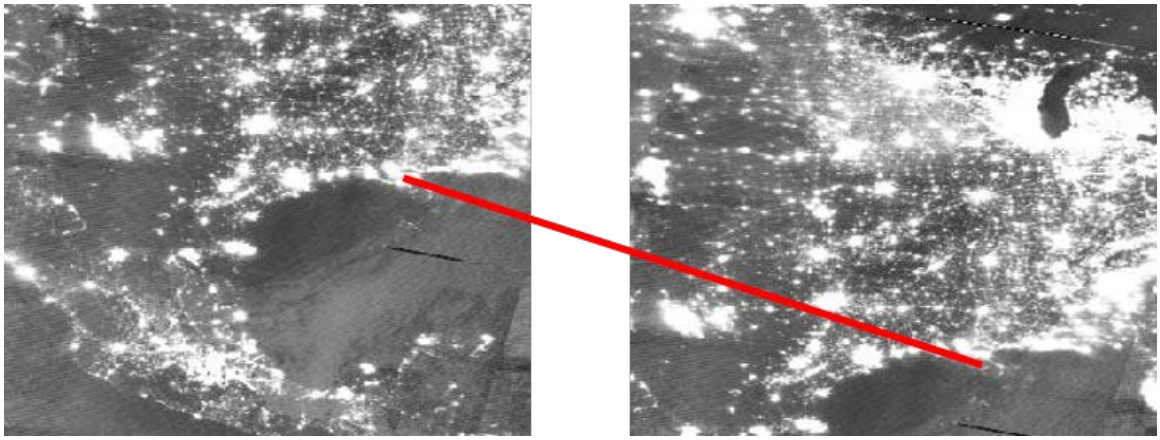

Figure 14. Mode 2: Comparing New Image to Previous Image, Finding New Orleans, LA, USA

The absolute pose is updated each iteration with the calculated relative pose between the two images in sequence, $\mathbf{T}_1^0$ described in Section 2.3.6,

$$\mathbf{T}_1 = \mathbf{T}_1^0 \mathbf{T}_0 \tag{3.2}$$

where $\mathbf{T}_1$ is the updated pose in the ECI frame and T_0 is the last estimate of the pose in the ECI frame. Remembering the pose is comprised of a rotation, $\mathbf{R}$, the transformation of the inertial frame to the updated camera frame, and a translation, $\mathbf{t}$, which is now the position of the camera in the inertial frame. A Direction Cosine Matrix, $\mathbf{C}$, (DCM) is usually between the spacecrafts body and orbital (RIC) frame to represent the attitude, a rotation can be done using $\mathbf{R}$ then converted to Euler angles [34]. The roll, pitch, and yaw data, as well as the translation was saved for each set of images.

$$\mathrm{C}_1 = \mathrm{R}_{\mathrm{body}}^{\mathrm{camera}} \mathrm{R}_1 \tag{3.3}$$

3.4 Converting Pixel Coordinates to Position Estimates

TIM operates by associating pixel coordinates from DNB to a Latitude and longitude, so the relationships between Llh, ECEF, and ECI frames must be illustrated. The pixel to Llh relationship is direct by adding in an approximate altitude, and then Llh can be converted to an XYZ coordinate from the center of the Earth in the ECEF frame. From here, supplementing with the time the picture was taken, the coordinate can be rotated into the ECI frame, giving an inertial coordinate that can be used in a state vector with a Kalman Filter.

3.4.1 Pixel to Llh

Black Marble's image resolution is 13500 x 6740 pixels. Knowing each pixel represents a square 742 m x 742 m plot of land, and there is no overlap between land cover, it can be assumed that

$$1 \text{ pixel} = \frac{180}{6750} \text{ degrees} = 0.02667^{\circ} \tag{3.4}$$

of both latitude and longitude.

3.4.2 Llh to ECEF and ECI

The Department of Defense World Geodetic System 1984 (WGS-84) is what is commonly used for satellite GPS position [35]. WGS-84 describes an oblate Earth, using Earth's equatorial radius, a, polar radius, b, the first eccentricity squared, e^2, and the flattening of the Earth, f [35].

$$a = 6378137 \text{ m}$$

$$b = 6356752.3142 \text{ m}$$

$$e^2 = 0.00669437999013$$

$$f = \frac{a - b}{a} = 1/298.257223563$$

The Earth's rotation rate, ω_E, and Earth's gravitational constant (GM) are also used [35].

$$\omega_E = 7.2921150 \times 10^{-5} \text{ rad/s}$$

$$GM = 3986004.418 \times 10^8 \text{ m}^3/\text{s}^2$$

The ECEF and ECI frames have a common origin of geocentric coordinates, where celestial and terrestrial latitude are the same, but different in geodetic coordinates, given by φ. Celestial longitude, λ, and terrestrial longitude, l are offset depending on time of day, shown as

$$\lambda - \lambda_0 = l - l_0 + \omega_E t \tag{3.5}$$

where t, is time, and λ_0 and l_0 are when $t = 0$ [35].

To model Earth as an ellipse for geodetic coordinates, the meridian radius of curvature, M, is

$$M = \frac{a(1 - e^2)}{(1 - e^2 \sin^2 \varphi)^{3/2}} \tag{3.6}$$

and helps find the latitude rate, V_N, or velocity in the North direction using the geodetic height, h [36].

$$V_N = (M + h)\dot{\varphi} \tag{3.7}$$

The radius of curvature in the vertical prime, $\bar{N}$, is used

$$\bar{N} = \frac{R}{\sqrt{1 - e^2(\sin^2 \varphi)^2}} \tag{3.8}$$

to find V_E, velocity in the East direction,

$$V_E(N + h)\cos(\varphi)\dot{l} \tag{3.9}$$

The projection of N on the x-y plane gives Cartesian position coordinates, and ECEF position can be calculated from geodetic coordinates by

$$r_{ECEF} = \begin{bmatrix} (N + h)\cos(\varphi)\cos(l) \\ (N + h)\cos(\varphi)\sin(l) \\ [N(1 - e^2) + h]\sin(\varphi) \end{bmatrix} \tag{3.10}$$

[35]

Furthering to ECI coordinates, a rotation angle, μ, is needed in addition to a rotation about the z-axis [35].

$$\mu = \lambda_0 - l_0 + \omega_E t \tag{3.11}$$

$$C_{ECEF}^{ECI} = \begin{bmatrix} \cos\mu & \sin\mu & 0 \\ -\sin\mu & \cos\mu & 0 \\ 0 & 0 & 1 \end{bmatrix} \tag{3.12}$$

3.5 Kalman Filters

Kalman filters are a filter estimator built off the idea of smoothers that filter out noise in measurements and use a best fit between them that can be applied real-time [36]. The process follows a state and covariance estimate extrapolation (propagation), filter gain computation, state and covariance estimate update. An EKF and UKF are specifically tailored for non-linear dynamical systems with continuous-time measurements [37].

3.5.1 Linear Kalman Filter

Given the system dynamics $\mathbf{\Phi}$ along with $\mathbf{x}_{\mathrm{k}}^{-}$, the state estimate, $\mathbf{P}_{\mathrm{k}}^{-}$, the covariance estimate, $\mathbf{y}_{\mathrm{k}}$, the measurement, $\mathbf{Q}_{\mathrm{k}}$ the process noise matrix, and $\mathbf{R}_{\mathrm{k}}$ the measurement noise covariance matrix, the Kalman Gain at the k-th time step, K_{k}, can be calculated as

$$\mathbf{K}_{\mathrm{k}} = \mathbf{P}_{\mathrm{k}}^{-}\mathbf{H}^{\mathrm{T}}(\mathbf{H}\mathbf{P}_{\mathrm{k}}^{-}\mathbf{H}^{\mathrm{T}} + \mathbf{R})^{-1} \tag{3.13}$$

.

The updated, or a posteriori state estimate is

$$\hat{\mathbf{x}}_{\mathrm{k}}^{+} = \hat{\mathbf{x}}_{\mathrm{k}}^{-} + \mathbf{K}_{\mathrm{k}}(\mathbf{y}_{\mathrm{k}} - \mathbf{H}\hat{\mathbf{x}}_{\mathrm{k}}^{-}) \tag{3.14}$$

and the a posteriori covariance

$$\mathbf{P}_{\mathrm{k}}^{+} = \mathbf{P}_{\mathrm{k}}^{-} - \mathbf{K}_{\mathrm{k}}\mathbf{H}\mathbf{P}_{\mathrm{k}}^{-} \tag{3.15}$$

where H is the measurement sensitivity matrix [37]. The system is then propagated from k to $\mathrm{k}+1$ with

$$\hat{\mathbf{x}}_{\mathrm{k+1}}^{-} = \mathbf{\Phi}_{\mathrm{k}}\hat{\mathbf{x}}_{\mathrm{k}}^{+} \tag{3.16}$$

and

$$\mathbf{P}_{\mathrm{k+1}}^{-} = \mathbf{\Phi}_{\mathrm{k}}\mathbf{P}_{\mathrm{k}}^{+}\mathbf{\Phi}_{\mathrm{k}}^{\mathrm{T}} + \mathbf{Q}_{\mathrm{k}} \tag{3.17}$$

3.5.2 Extended Kalman Filter

The position estimator will rely on the use of an EKF based on its use in contemporary literature, as well as the specific application using the camera frame described by Straub [32]. Attempting to write the process in sequential order for an EKF, it is formulated by first defining the system dynamics as

$$\dot{\mathbf{x}} = f(\mathbf{x}, t) \tag{3.18}$$

and the covariance matrix, $\mathbf{P}$, is able to be propagated by

$$\dot{\mathbf{P}} = \mathbb{F}\mathbf{P} + \mathbf{P}\mathbb{F}^{\mathrm{T}} + \mathbf{Q} \tag{3.19}$$

where

$$\mathbb{F}(t) = \left.\frac{\partial f(\mathbf{x}, t)}{\partial \mathbf{x}}\right|_{(\mathbf{x}=\mathbf{x}^*)} \tag{3.20}$$

and $\mathbf{Q}$ is the process noise. It is evaluated at the expected values of the state dynamics [32]. The measurement $\mathbf{y}$, is related to the state vector by the relation

$$\mathbf{y} = \bar{h}(\mathbf{x}, t) \tag{3.21}$$

Letting $\mathbf{H}$ be the Jacobian of this relationship, also known as the measurement sensitivity matrix,

$$\mathbf{H} = \left.\frac{\partial h}{\partial \mathbf{x}}\right|_{(\mathbf{x}=\hat{\mathbf{x}})} \tag{3.22}$$

.

This is found using the Line of Sight measurements, s, by using the Inertial to Camera rotation $\mathrm{R}_{\mathrm{CAM}}^{\mathrm{ECI}}$, and the dot product of the unit vectors in the inertial frame, $\hat{\mathbf{e}}$,

$$\mathbf{H}_{\mathrm{k}} = \mathbf{R}_{\mathrm{CAM}}^{\mathrm{ECI}} \frac{1}{||\mathrm{s}_{\mathrm{k}}||} [\hat{\mathbf{e}}_{\mathrm{kECI}} \hat{\mathbf{e}}_{\mathrm{kECI}}^{\mathrm{T}} \text{ - } \mathbf{I}_{3\mathrm{x}3} \quad \mathbf{0}_{3\mathrm{x}3}] \tag{3.23}$$

[32].

The vector $\mathbf{R}_{\mathrm{CAM}}^{\mathrm{ECI}}$ matrix is determined by assuming the attitude at the time the image was taken is known. At this point the measurement noise covariance, $\mathbf{R}$ is needed and determined as

$$\mathbf{R} = \sigma^2 (\mathbf{I}_{3\mathrm{x}3} \text{ - } \bar{\mathbf{e}}_{\mathrm{kC}} \mathbf{e}_{\mathrm{kC}}^{\mathrm{T}}) \tag{3.24}$$

where σ is taken to be one thousand times the accuracy of a star tracker [32]. For the Kalman gain and using the measurement, determine the residual to be

$$\boldsymbol{\nu}_{\mathrm{k}} = \mathbf{y}_{\mathrm{k}} \text{ - } h(\mathbf{x}_{\mathrm{k}}, t_{\mathrm{k}}) \tag{3.25}$$

The Kalman gain for the system can be calculated as

$$\mathbf{K}_{\mathrm{k}} = \mathbf{P}_{\mathrm{k}}^{\text{-}} \mathbf{H}_{\mathrm{k}}^{\mathrm{T}} (\mathbf{H}_{\mathrm{k}} \mathbf{P}_{\mathrm{k}}^{\text{-}} \mathbf{H}_{\mathrm{k}}^{\mathrm{T}} + \mathbf{R}_{\mathrm{k}})^{\text{-}1} \tag{3.26}$$

where $\mathbf{P}$ is the expected mean squared error, covariance [32]. The current state estimate can be updated using this gain and the residual

$$\hat{\mathbf{x}}_{\mathrm{k}}^{+} = \hat{\mathbf{x}}_{\mathrm{k}}^{\text{-}} + \mathbf{K}_{\mathrm{k}} (\mathbf{y}_{\mathrm{k}} \text{ - } \mathbf{H}_{\mathrm{k}} \hat{\mathbf{x}}_{\mathrm{k}}^{\text{-}}) \tag{3.27}$$

The a posteriori covariance must also be updated as

$$\mathbf{P}_{\mathrm{k}}^{+} = \mathbf{P}_{\mathrm{k}}^{\text{-}} \text{ - } \mathbf{K}_{\mathrm{k}} \mathbf{H}_{\mathrm{k}} \mathbf{P}_{\mathrm{k}}^{\text{-}} \tag{3.28}$$

3.5.3 Unscented Kalman Filter

The UKF is for applying a Kalman filter to a nonlinear discrete time system

$$\mathbf{x}_{k+1} = f(\mathbf{x}_k, \mathbf{u}_k, \mathbf{v}_k, k), \mathbf{y}_k = h(\mathbf{x}_k, \mathbf{u}_k, k) + \mathbf{w}_k \tag{3.29}$$

A set of points (sigma points, $\boldsymbol{\chi}$) are deterministically selected such that their mean and covariance match that of the probability density function of the state [37]. There are 2n+1 sigma points and associated weights; points are chosen in the classic UKF to match first two moments [37].

$$\boldsymbol{\chi}^m = \bar{\mathbf{x}},\ W_0 = \frac{\varkappa}{n+\varkappa} \tag{3.30}$$

$$\boldsymbol{\chi}_i^m = \bar{\mathbf{x}} + (\sqrt{(n+\varkappa)\mathbf{P}_{xx}})_i,\ W_i = \frac{1}{2(n+\varkappa)} \tag{3.31}$$

$$\boldsymbol{\chi}_{i+n}^m = \bar{x} - (\sqrt{(n+\varkappa)\mathbf{P}_{xx}})_i,\ W_{i+n} = \frac{1}{2(n+\varkappa)} \tag{3.32}$$

Each sigma point is propagated through the dynamics

$$\boldsymbol{\chi}_{k|k-1}^{(i)} = f(\boldsymbol{\chi}_{k|k-1}^{(i)}) \tag{3.33}$$

which are averaged to find a predicted mean,$\hat{\bar{\mathbf{x}}}_k^-$), and used to compute a covariance

$$\mathbf{P}_{xx,k}^- = \sum_{i=0}^{2n} W_i^c(\boldsymbol{\chi}_{k|k-1}^{(i)} - \hat{\bar{\mathbf{x}}}_k^-)(\boldsymbol{\chi}_{k|k-1}^{(i)} - \hat{\bar{\mathbf{x}}}_k^-)^T + \mathbf{Q}_{k-1} \tag{3.34}$$

Now, considering residual information and transforming the sigma points to observations gives:

$$\mathbf{\Gamma}^{(\mathrm{i})}_{\mathrm{k|k\text{-}1}} = h(\boldsymbol{\chi}^{(\mathrm{i})}_{\mathrm{k|k\text{-}1}}) \tag{3.35}$$

The transformed sigma points are averaged to determine an expected measurement

$$\hat{\mathbf{Y}}_{\mathrm{k}} = \sum_{\mathrm{i}=0}^{2\mathrm{n}} \mathrm{W}^{\mathrm{m}}_{\mathrm{i}} \mathbf{\Gamma}^{(\mathrm{i})}_{\mathrm{k|k\text{-}1}} \tag{3.36}$$

Having an expected measurement, the predicted observation covariance can be determined as:

$$\mathbf{P}_{\mathrm{yy,k}} = \sum_{\mathrm{i}=0}^{2\mathrm{n}} \mathrm{W}^{\mathrm{c}}_{\mathrm{i}} (\Gamma^{(\mathrm{i})}_{\mathrm{k|k\text{-}1}} - \hat{\mathbf{Y}}^{\text{-}}_{\mathrm{k}})(\Gamma^{(\mathrm{i})}_{\mathrm{k|k\text{-}1}} - \hat{\mathbf{Y}}^{\text{-}}_{\mathrm{k}})^{\mathrm{T}} + \mathbf{R}_{\mathrm{k}} \tag{3.37}$$

with the predicted cross covariance as follows:

$$\mathbf{P}_{\mathrm{xy,k}} = \sum_{\mathrm{i}=0}^{2\mathrm{n}} \mathrm{W}^{\mathrm{c}}_{\mathrm{i}} (\boldsymbol{\chi}^{(\mathrm{i})}_{\mathrm{k|k\text{-}1}} - \hat{\bar{\mathbf{x}}}^{\text{-}}_{\mathrm{k}})(\mathbf{\Gamma}^{(\mathrm{i})}_{\mathrm{k|k\text{-}1}} - \hat{\mathbf{Y}}^{\text{-}}_{\mathrm{k}})^{\mathrm{T}} \tag{3.38}$$

.

Finally, the standard Kalman Filter update can be applied

$$\boldsymbol{\nu} = \mathbf{Y} - \hat{\mathbf{Y}}_{\mathrm{k}} \tag{3.39}$$

$$\mathbf{K}_{\mathrm{k}} = \mathbf{P}_{\mathrm{xy}} \mathbf{P}^{\text{-}1}_{\mathrm{yy}} \tag{3.40}$$

$$\hat{\bar{\mathbf{x}}}^{+}_{\mathrm{k}} = \hat{\bar{\mathbf{x}}}^{\text{-}}_{\mathrm{k}} + \mathbf{K}_{\mathrm{k}} \boldsymbol{\nu} \tag{3.41}$$

$$\mathbf{P}^{+}_{\mathrm{xx,k}} = \mathbf{P}^{\text{-}}_{\mathrm{xx,k}} - \mathbf{K}_{\mathrm{k}} \mathbf{P}_{\mathrm{yy}} \mathbf{K}^{\mathrm{T}}_{\mathrm{k}} \tag{3.42}$$

3.6 Summary

This chapter defined the architecture of TIM for each of its modes. The scenario described using Suomi NPP TLE information to simulate its orbit and both Black Marble and VIIRS to replicate what it sees. Techniques were pulled across the aerospace and electrical engineering disciplines, utilizing methods of orbit propagation, satellite design, cartography, computer vision, and filtering. The simulations varied in time of year, length, and quality of data. The next chapter will discuss the results of these test cases, the obstacles faced, and how they were solved.

IV. Results and Analysis

4.1 Overview

MATLAB and OpenCV were used to integrate terrestrial light data and lay the foundation to create a real-time TIM algorithm for successful position and attitude determination. The goals of the different test cases described in the following sections are to understand how to set up a simulation that can be read into TIM to conduct the two modes of operation. Mode 1: Position Estimation attempts balance getting good measurements with getting enough measurements for the filter to operate properly over time. Mode 2: Attitude Determination attempts to discover the proper process for recovering the pose of these image types taken from space The first section will present an analysis and discussion of the many popular OpenCV algorithms described in Section 2.3, and why SIFT was chosen for Mode 1 and Mode 2 operation. Next, an extensive analysis of Mode 1 is completed, followed by a preliminary study of Mode 2. Mode 1 was employed in two test cases, each using simulations of Woman and Veteran data. Each test case computes the errors in three settings, the strict error of the measurement, the error driven down with the use of an EKF, and the error driven down with the use of an UKF. Mode 2 shows significantly strong matches in a sequence of images, and uses the calculation of the pose to find Euler angles over time. Finally, a summary of the collaborative work will tie the results together in a conclusion.

4.2 Comparing Feature Detection Algorithms

This section will highlight the algorithms in OpenCV tested image sets for Italy, the Great Lakes, the Gulf of Oman, India, and South East Asia. The success rates of actual city matches can be found in Table 3. No outlier rejection using RANSAC

was conducted, but of the results in the 60%-70% success range, it would make a considerable difference. Black Marble was used at half its true resolution for a faster processing time, and so were the successive images. Some algorithms, such as SIFT, have their own thresholding built-in, but no internal parameters of the algorithms were changed. Acceptable matches were found using Lowe's Ratio Test, set at 0.7 distance for all tests. A higher Lowe's Ratio means that more matches are retained, a lower value implies more precision. During evaluation of multiple algorithms, an observation was noted that BRIEF was significantly slower than others being evaluated.

Table 3. OpenCV Algorithms and test results on the five image sets to a database

Test	Feature	Descriptor	Matching	Italy	Gulf	Great Lakes	India	South East Asia
1.1.1	MSER	BRIEF	BF	43%	0%	0%	50%	100%
1.1.2	MSER	BRIEF	FLANN	43%	100%	0%	67%	100%
1.2.1	MSER	FREAK	BF	0%	0%	67%	0%	25%
1.2.2	MSER	FREAK	FLANN	0%	50%	53%	0%	33%
2.1.1	FAST	BRIEF	BF	50%	43%	50%	60%	50%
2.1.2	FAST	BRIEF	FLANN	60%	50%	24%	50%	50%
2.2.1	FAST	FREAK	BF	5%	7%	0%	50%	0%
2.2.2	FAST	FREAK	FLANN	0%	0%	3%	40%	10%
3.1	SIFT		BF	75%	100%	88%	88%	86%
3.2	SIFT		FLANN	78%	91%	95%	93%	90%
4.1	SURF		BF	58%	94%	93%	90%	84%
4.2	SURF		FLANN	60%	94%	89%	84%	93%
5.1	BRISK		BF	78%	90%	92%	100%	88%

A visual result of Test 1.2.1 MSER/FREAK is shown in Figure 15. MSER is the only feature detector that works in regions and blobs, called hulls, rather than keypoints. For this to actually give keypoints on which the rest of the algorithm relies, FAST was applied and picked up the centroids of the city lights. Using the regions and hulls as features in the image did not increase the success rate of the algorithm, but this particular test matched Chicago perfectly.

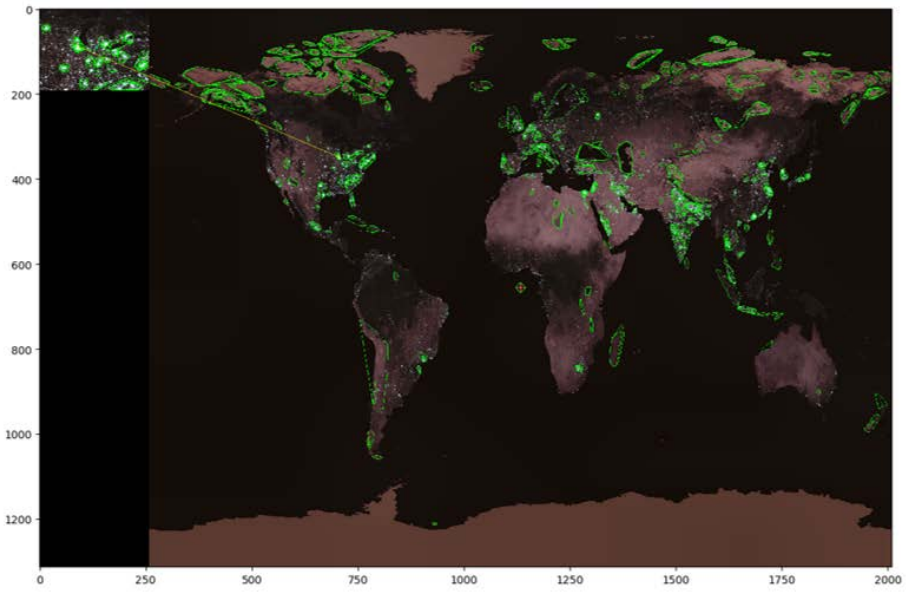

Figure 15. MSER - FREAK Test on Black Marble

For all future results, SIFT was used for both feature detection and descriptor generation in conjunction with FLANN. This was chosen because it is a common pairing in visual navigation works, and had a high average success rate in Table 3. The maximum number of features for Black Marble was set at 2000 with 5 octave layers and for FOV images at 1000 and 3 octave layers in order to reduce computation time. Both had a contrast threshold of 0.01 and an edge threshold of 10 to particularly focus on bright city lights. FLANN had no extra conditions set on it and was used at factory settings. RANSAC specifically works with the matching

process, and uses the Essential, Fundamental, or Homography matrix mask to pick out the strongest matches in a list. The mask describes the coordinates that satisfy the epipolar constraint (Equation 2.6) the best.

The Homography matrix was a technique explored in updated TIM schemes that solves the epipolar constraint equation by assuming both images are in the same plane and keep the same attitude. It does a perspective transformation in a way that the back-projection error is minimized. Rather than matching coordinates, it is able to match areas shown in Figure 16 that resemble the red FOV boxes the simulation was created from.

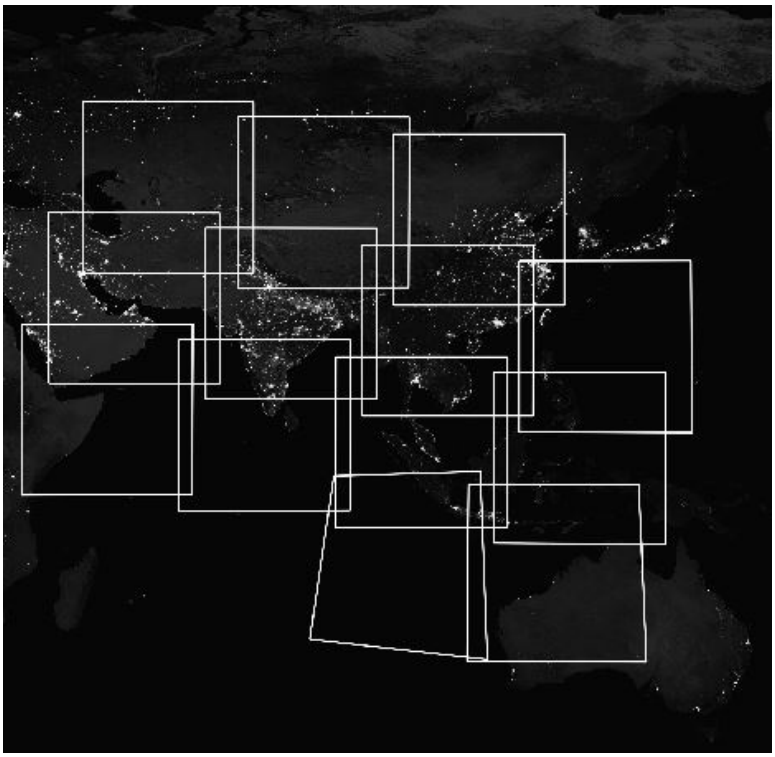

Figure 16. Find Homography Test on Woman Data - Accurate FOV prediction

4.3 Mode 1: Position Estimation

The simulation will generate images from the measurement type, Black Marble or Worldview, that are down-sampled from the composite by a factor of 2, which creates

some random blurring of pixels. It accomplishes this by setting the following initial parameters:

- length of time of simulation (1 hour or 24 hours)
- time passed between image acquisition (300 seconds)
- FOV of the camera (3000 km x 3000 km)
- TLE used (Woman or Veteran)
- measurement type (Black Marble or Worldview)

The TLE is propagated through the 2BP to simulate an orbit in the inertial frame, which was translated to pixel coordinates in the composite. The FOV is plotted on the composite, and each FOV is saved as an individual image. The method ensured there was no stretching of pixels and images were only collected during nighttime operation of Suomi NPP. SIFT/FLANN in Figure 17 below shows an example of what many correct matches look like, with just one outlier that could have been solved by applying RANSAC.

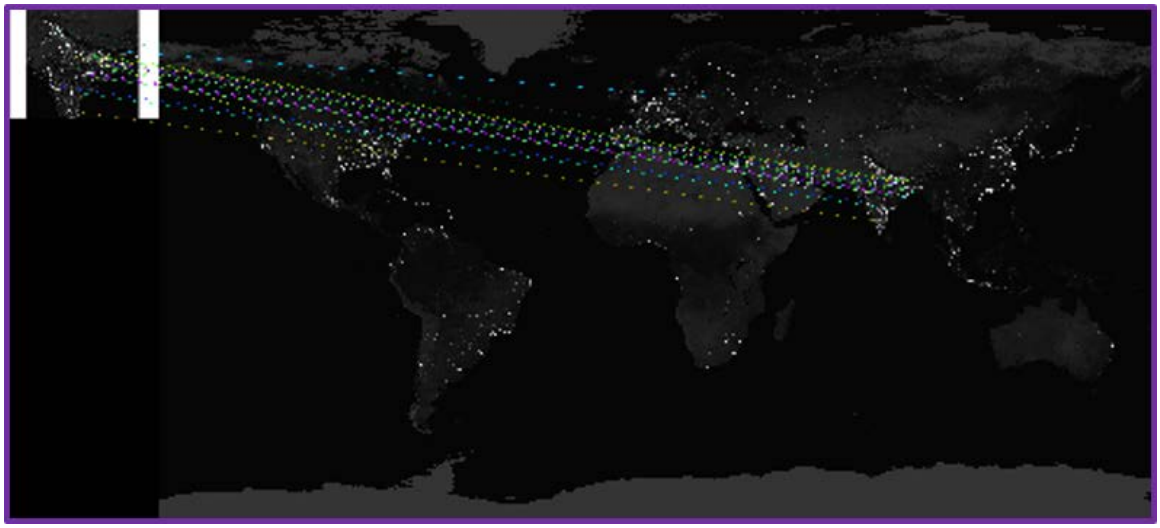

Figure 17. SIFT Test for India

These image measurements were read into TIM and matched sequentially to Black Marble. There was no truth information given to TIM to estimate position of the satellite at a point in time. These were saved as pixel coordinate matches between the measurement and Black Marble. The match coordinates in the measurement were averaged, and a vector calculated from the average match to the center of the image, shown in Figure 18.

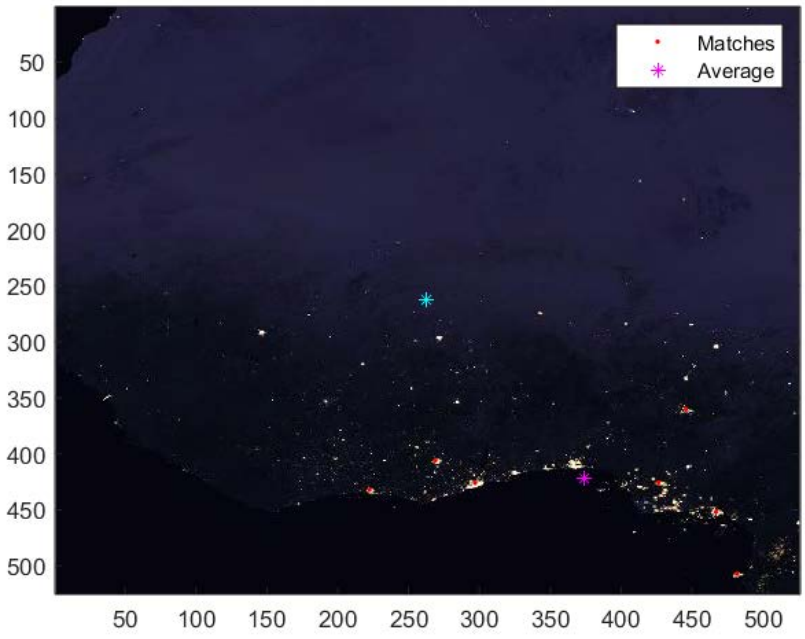

Figure 18. Average of Strong Matches in Northern Africa

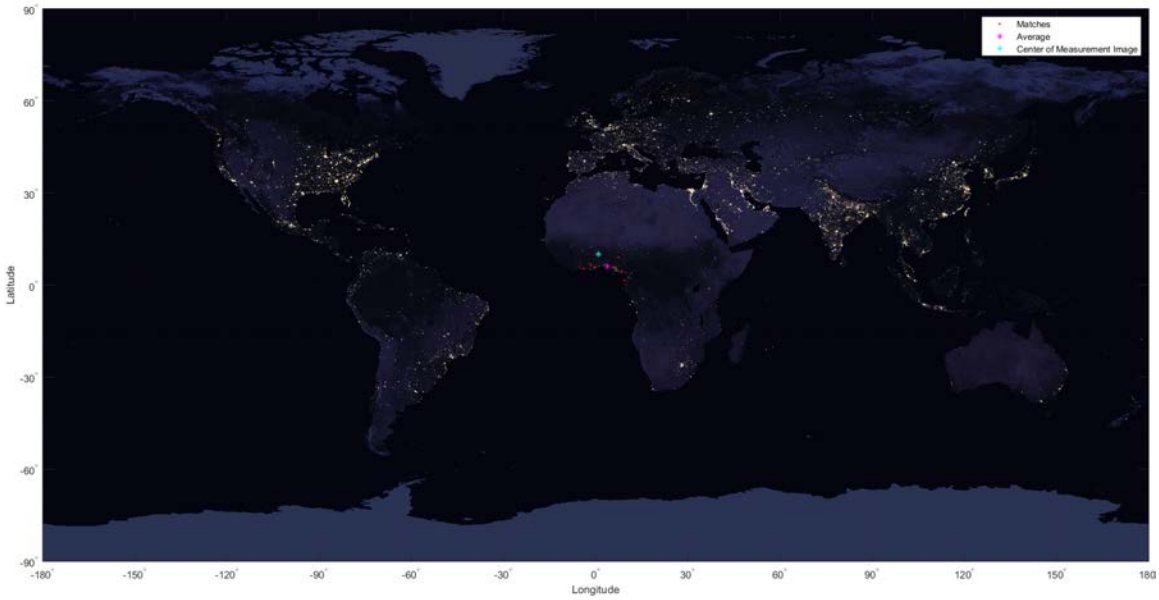

Figure 19. Average of Strong Matches in Northern Africa, calculated on Black Marble

The match coordinates in Black Marble were also averaged in Figure 19, and a vector to the center of the measurement image from the average value was solved for. This average-to-center vector was applied to Black Marble's match to determine TIM's estimate for the position. Once a pixel coordinate is found, it can be converted to a latitude and longitude. The expected altitude of the satellite and its velocity are supplied as measurements from other sources and the coordinates are rotated into the ECEF and ECI frames. This process gives a full inertial state vector of position and velocity that can then be used to employ a Kalman Filter. Error in position estimates are given for the test cases without any filtering, with an EKF, and finally with a UKF.

Table 4. Test Cases and their Success with Filters

Time	TLE	Area	RANSAC	None	EKF	UKF
1 hour	Woman	EU		✓	✓	✓
			✓	✓	✓	✓
	Veteran	USA		✓	✓	✓
			✓	✓	✓	x
		Asia		✓	✓	✓
			✓	✓	✓	✓
24 hours	Woman			✓	✓	x
			✓	✓	✓	x
	Veteran			✓	✓	x
			✓	✓	✓	x

Due to varying passage of time between measurement updates, results are not always attained for these cases. The situation for each case is described in Table 4 and discussed in the following sections, where a checkmark means a test was done and an x means the test did not give any results. These only occurred in filter usage, usually where the Cholesky matrix computation could not be completed. The beginnings of this work test short datasets, only 4-5 images, to good results, shown in Figures 20 and 21. The rest of this section will discuss the Woman and Veteran datasets for one nighttime pass, and the second half will discuss a full 24 hour simulation.

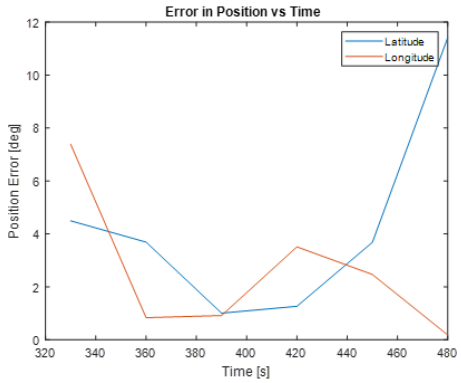

Figure 20. Woman, only 4 images

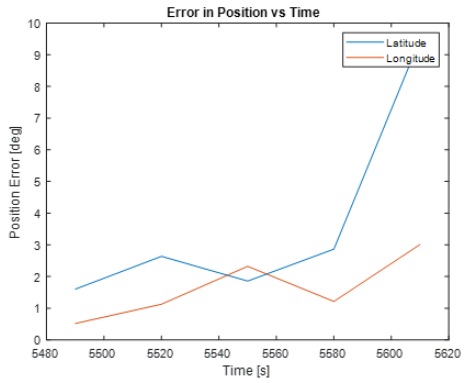

Figure 21. Veteran, only 4 images

This section will continue the discussion on using city lights for accurate position estimation during on-orbit operation. As the first attempt of this type of capability, the aim is on proving the feasibility of future exploration with preliminary results.

4.3.1 Test Length: One Nighttime Pass

A single nighttime pass case was done in order to test the usability of filters between image acquisition. The length of one nighttime pass comes out to about an hour, which is a little less than half Suomi NPP's period. The time step between calculations is 5 seconds, with an image measurement available every 300 seconds. With 9 images available for each test case, not every image is usable, due to overflight of water or unpopulated areas. Furthermore, when RANSAC is applied it rejects images that only have weak matches by finding the mask of the Homography matrix, or the transformation between images. Therefore if an image does not match strongly with Black Marble, it is rendered useless. Table 5 shows how many images are usable in each dataset with No Outlier Rejection (No OJ), with outlier rejection (RANSAC) and how many images total there are.

Table 5. Usability of Short Image Sequence

Data	No OJ	RANSAC	Total Images
Woman - EU	6	5	9
Veteran - USA	6	5	9
Veteran - Asia	6	5	9

4.3.1.1 No Filtering

For only an hour of the Woman data, we can see a difference that RANSAC makes. The very first measurement, which can set the tone for filter usage, it has almost 50° error in latitude and much more than that in longitude, looking at Figure 22. The rest of the images in sequence are spot on, so those make it through the outlier rejection process can be considered strong measurements. A very similar sentiment is verified with the following two cases from Veteran data. These results show the necessity of outlier rejection.

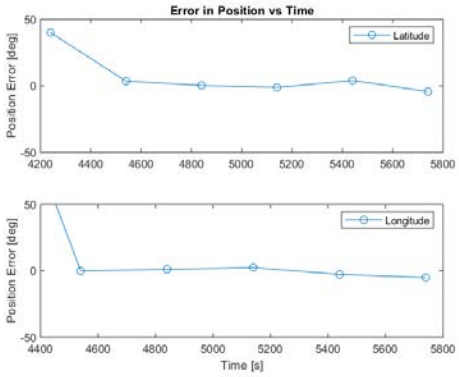

Figure 22. Short Run Woman (No RANSAC/No Filter)

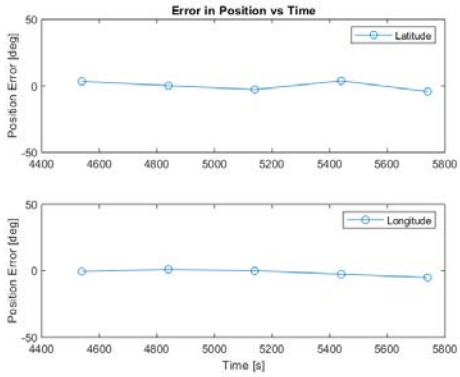

Figure 23. Short Run Woman (RANSAC/No Filter)

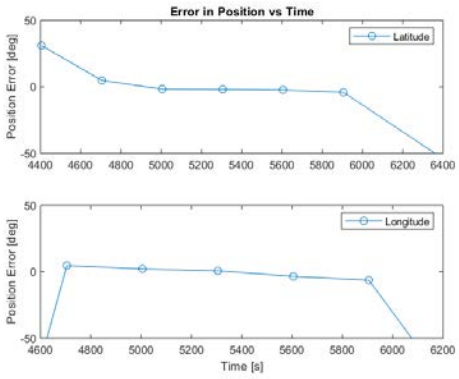

Figure 24. Short Run Veteran USA (No RANSAC/No Filter)

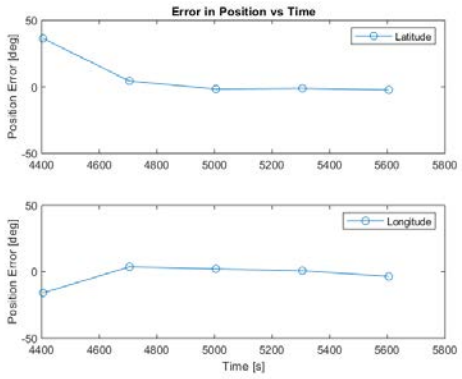

Figure 25. Short Run Veteran USA (RANSAC/No Filter)

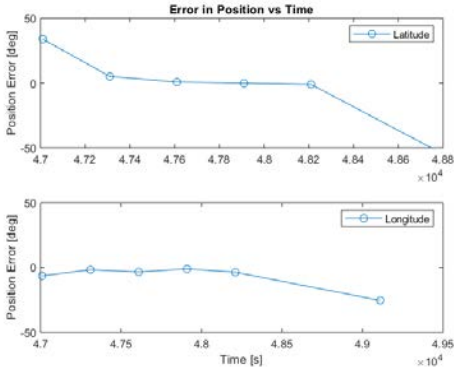

Figure 26. Short Run Veteran ASIA (No RANSAC/No Filter)

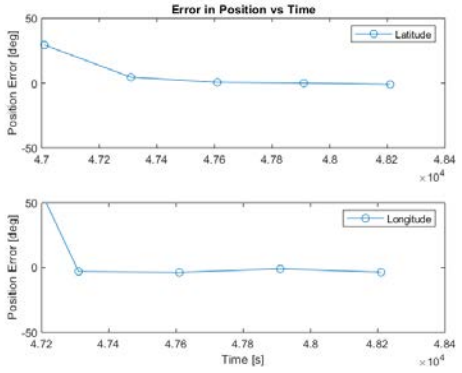

Figure 27. Short Run Veteran ASIA (RANSAC/No Filter)

4.3.1.2 EKF

Getting into the first of the filters, the EKF from Straub's paper is replicated [32]. The propagation scheme is not terribly robust, and there are numerous issues with observability due to the measurement only providing a latitude and longitude, but a full state vector having position and velocity in the inertial frame. The σ chosen for this simulation was one thousand times 18 arcseconds, the standard accuracy of a star tracker. The process noise, Q, was set at 0.7502 across a 6x6 matrix along the diagonal, which keeps the Kalman Gain from being singular, at 0.7.

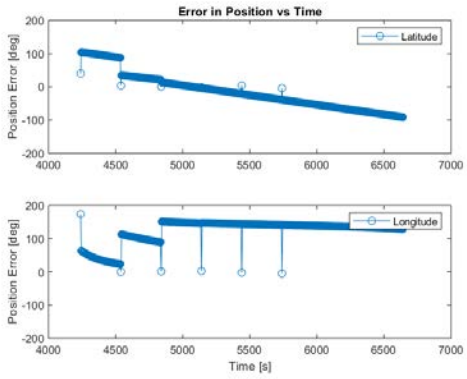

Figure 28. Short Run Woman (No RANSAC/EKF)

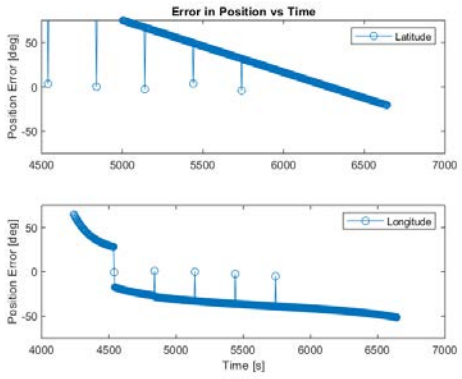

Figure 29. Short Run Woman (RANSAC/EKF)

In any of the cases, the propagation scheme is not ever corrected by the measurements, and it seems there is something off with the filter, such as, possibly, the update being improperly applied. This could be due to the fact that the H matrix is not simply a rotation matrix for this particular nonlinear case. The measurements acquired are a latitude, longitude coordinate, but the ECI coordinate is backed out, and it is re-rotated into a camera frame. This means the coordinate that engages with the filter is a unit vector.

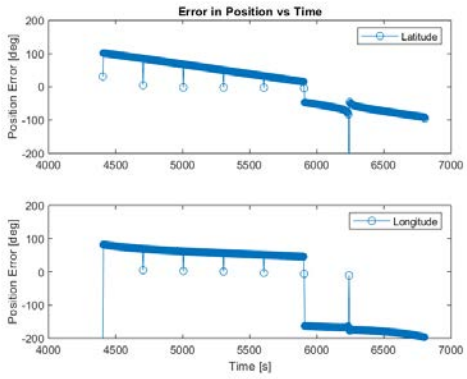

Figure 30. Short Run Veteran USA (No RANSAC/EKF)

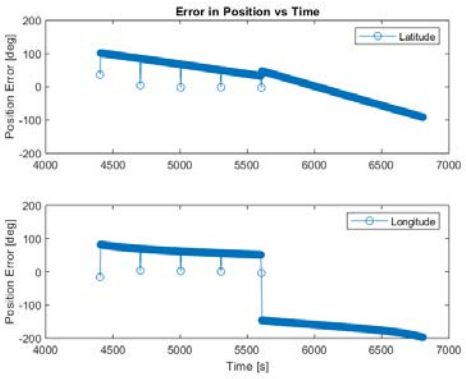

Figure 31. Short Run Veteran USA (RANSAC/EKF)

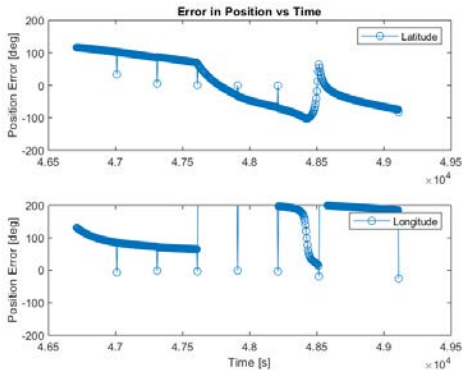

Figure 32. Short Run Veteran ASIA (No RANSAC/EKF)

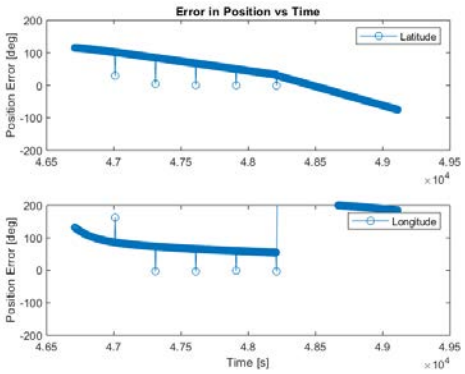

Figure 33. Short Run Veteran ASIA (RANSAC/EKF)

4.3.1.3 UKF

The nonlinear transformation for the observation function is a better fit for an UKF, because it is more robust for nonlinear systems than the EKF. The use of a UKF was not found in the literature like an EKF, so it was applied precisely with the latitude and longitude coordinate. The tuning values were set as follows:

$$\alpha = 0.001$$

$$\beta = 2$$

$$\varkappa = 0$$

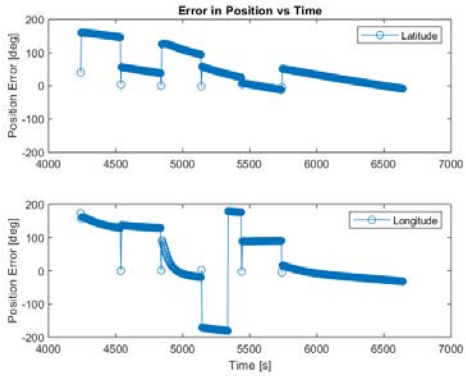

Figure 34. Short Run Woman (No RANSAC/UKF)

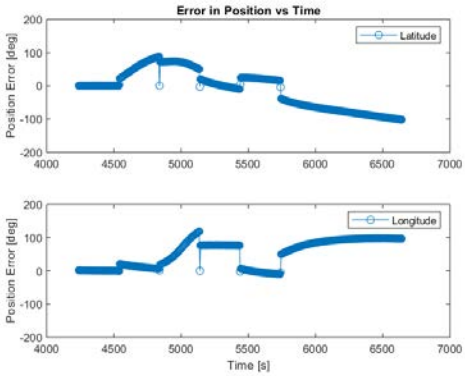

Figure 35. Short Run Woman (RANSAC/UKF)

The errors in latitude in Figure 34 appear to drive to zero as time continues, however this is not the case for the version with RANSAC applied. The propagation scheme is still not properly updated by the measurement with little error, despite using a different propagation scheme than that of the EKF.

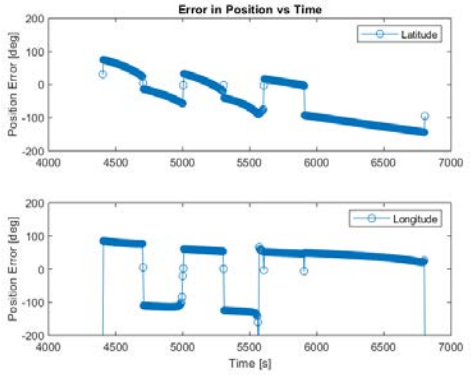

Figure 36. Short Run Veteran USA (No RANSAC/UKF)

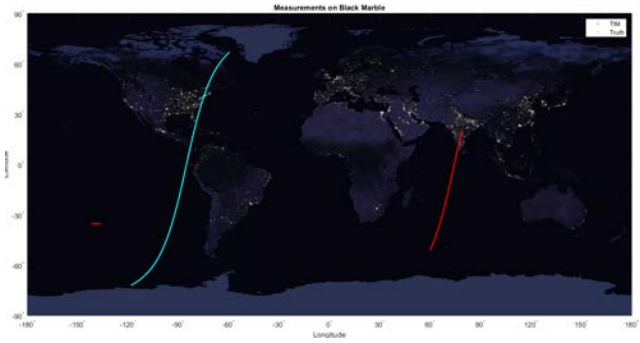

Figure 37. Short Run Veteran USA (RANSAC/EKF/Ground Track)

Above in Figure 37 the blue line shows the true orbit that was propagated in the simulation. This is what the image measurements were taken from, and as such, small red dots can be seen indicating TIM identified the position very close to the truth. Those red dots correlate with Figure **??** at almost zero error. It is further shown that the propagation scheme in the filter is not taking the update from the images at all when looking at the red line continuing on its path from India. Looking at only Figure 36, it would be tempting to think there is only an error in calculation of longitude, but actually looking at the errors in latitude and longitude this would not be the case.

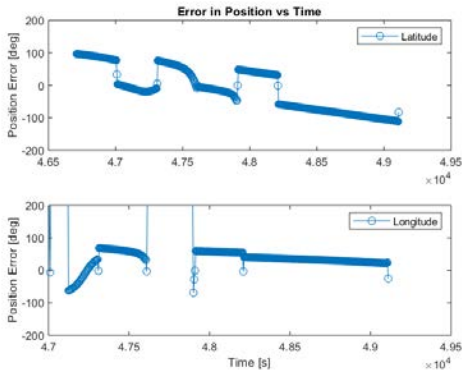

Figure 38. Short Run Veteran ASIA (No RANSAC/UKF)

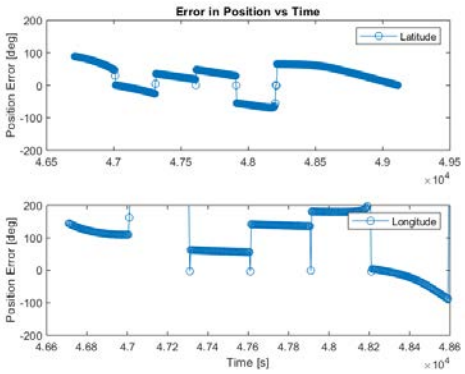

Figure 39. Short Run Veteran ASIA (RANSAC/UKF)

Figure 34 shows around 180° of error in longitude, which could suggest wrapping issues. Remembering Figure 37, there could be issues with the calculations of latitude and longitude coordinates from the 2BP propagation. This is unlikely, as it uses the same process as the simulation, but would be worth looking into for further use of the filters.

4.3.2 Test Length: 24 hours

A 24 hour simulation was performed in order to test the usability of filters between image acquisition, and during daytime operations. This results in full-coverage of the Earth, which is what Suomi NPP's orbit was designed for. The simulation will undergo sixteen periods, and only take images during nighttime operations, giving sixteen 45-minute passes of the Earth. The time step between calculations is 5 seconds, with an image measurement available every 300 seconds during nigghtime passes. With 136 images available for each test case, not every nighttime image is usable, due to overflight of water or unpopulated areas. Furthermore, when RANSAC is applied once again with the mask of the Homography matrix and rejects images that do not match strongly with Black Marble.

Table 6. Usability of Long Image Sequence

Data	No OJ	RANSAC	Total Images
Woman	84	81	136
Veteran	79	52	136

4.3.2.1 No Filtering

The most exciting thing to visualize is where these measurements are popping up around the Earth, shown in Figure 40. Every time the measurement image is processed, its ECEF coordinate is plotted on the globe. This acts as a sanity-check for the image processing scheme, and shows the distribution of good measurements across land in a different way. From looking at this, it is easy to tell the best measurements come over what is known as the most populated areas, especially near unique bodies of water. The images in either simulation tend to be most precise over the Great Lakes, the Gulf of Guinea, the Persian Gulf, the Mediterranean, and South East Asia.

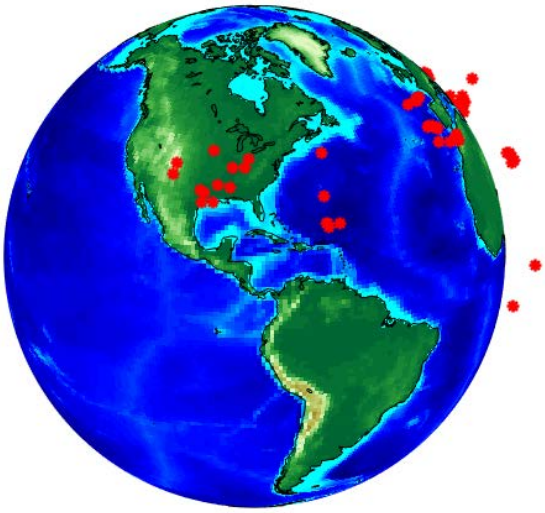

Figure 40. Results of TIM in ECEF Coordinate Frame for Woman Data - No Filter

This is able to be seen in conjunction with the error charts in Figures 44. Every blue dot correlates with a red star in Figure 40 and in Figure 43.

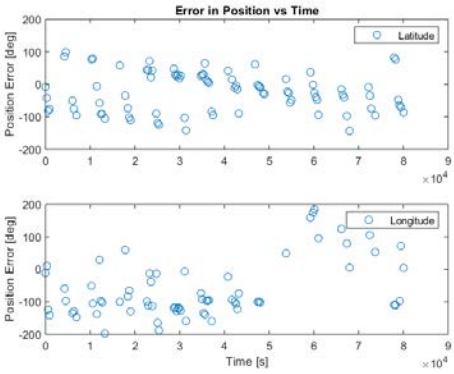

Figure 41. Woman (No RANSAC/No Filter)

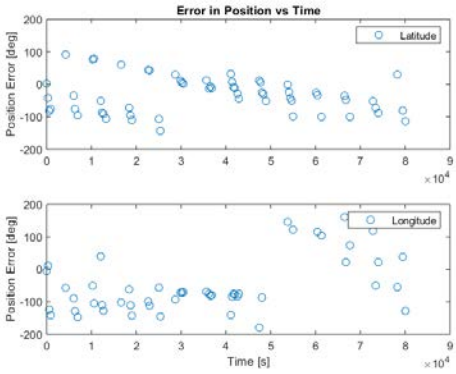

Figure 42. Woman (RANSAC/No Filter)

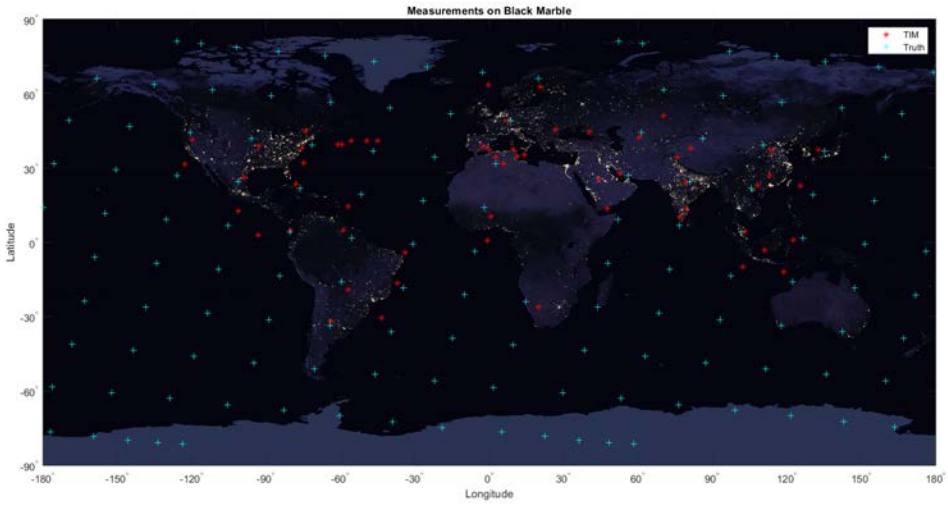

Figure 43. Ground Track of Woman (RANSAC/No Filter)

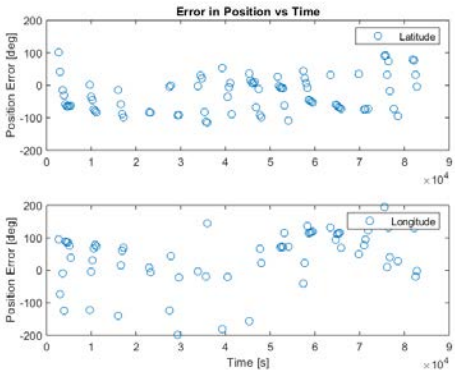

Figure 44. Veteran (No RANSAC/No Filter)

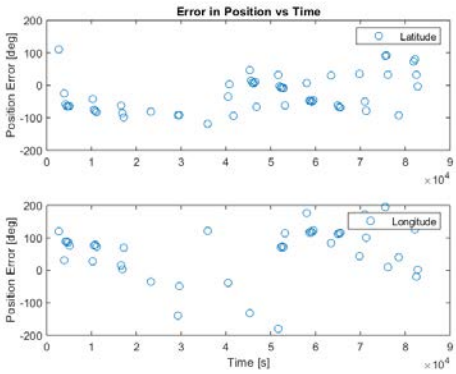

Figure 45. Veteran (RANSAC/No Filter)

4.3.2.2 EKF

The filter usage had many problems during short simulations, and running during a 45-minute daytime pass blew up the error in interesting ways. The latitude in both cases followed a choppy oscillating path for about half the simulation, and the longitude followed a tangent wave. The cause of this was improper coding of these filters, with the first clue being the covariance (not shown) in both cases went out of control almost immediately.

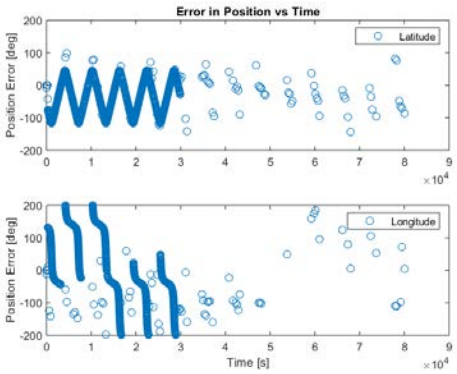

Figure 46. Woman (No RANSAC/EKF)

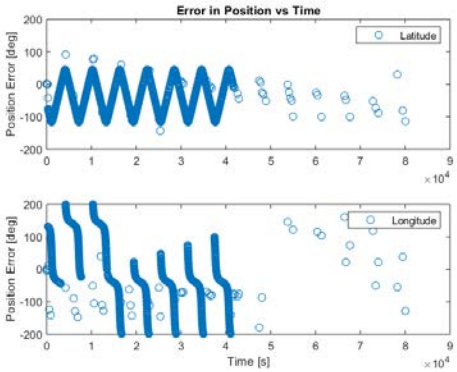

Figure 47. Woman (RANSAC/EKF)

The Woman data began at the Cape of South Africa heading south, so it begins with no measurement update for almost an hour before on is finally available over the Baltics. it is very interesting that the front half of the Woman data and the second half of the Veteran data followed the sine wave pattern so intensely. This suggests problems with the conversion from latitude and longitude coordinates to the inertial state vector required for filter usage. A suggestion for future work would be to look at mean errors or the absolute value of errors to verify this is the problem. Due to the immediate rupture of filter usage in both cases, the UKF was not able to function properly through the entirety of a day. Changing tuning values did not affect its ability to iterate through the images, so no results of a 24 hour simulation with an UKF are reported.

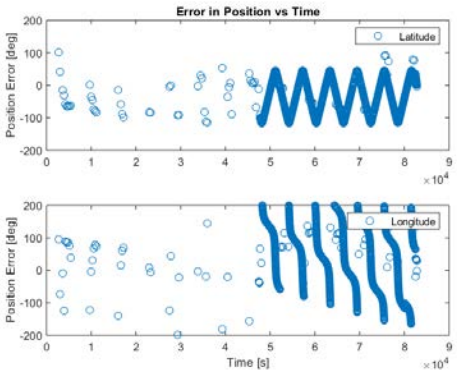

Figure 48. Veteran (No RANSAC/EKF)

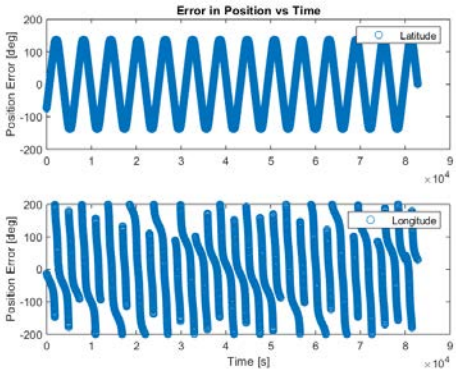

Figure 49. Veteran (RANSAC/EKF)

4.3.3 Summary

RANSAC rendered an average of 11% of all images and 17% of usable images in a sequence unusable as a measurement when it at least had one good match Lowe's Ratio test. This further complicates filter operation since long periods of time without a measurement can cause the covariance to break the filter. A better option would be to tune the confidence in the measurements that make it through RANSAC rather than keeping the variance of the measurement a constant. Another problem with the filter is with matrix observability. Observability is a quality of a system that describes how well the state vector can be constructed from its outputs. The state vector in this case is an inertial coordinate with three components and an inertial velocity component with three components.While the velocity is provided as if from another sensor (with its own sensor noise), a latitude and longitude coordinate will only ever be two components, and cannot give any information on altitude. This leads nicely to our next section on attitude determination, because the methods used for attitude determination are tools for stereoscopic vision. When two images are presented of the same feature from different points-of-view, it is possible to measure the distance of the feature from the camera, giving depth, or altitude.

4.4 Mode 2: Attitude Determination

The attitude of an object can be found using visual odometry, tracking the pose change in a sequence of images. If the first image is assumed to be at position (origin at (0,0) and with the identity matrix as its attitude, the pose calculated in the second image will be a direct map to the origin. The third image can find the pose between it and the second, but by using the pose to the origin, can find the pose from the third to the origin. This experiment was conducted with a sequence of 30 images in a 2D environment. The path was a straight line for 10 feet, a right turn and a left turn and continuing straight again. Given a scaling value of 1 foot between images, a primitive model of TIM Mode 2 was able to plot this path, shown in Figure 50.

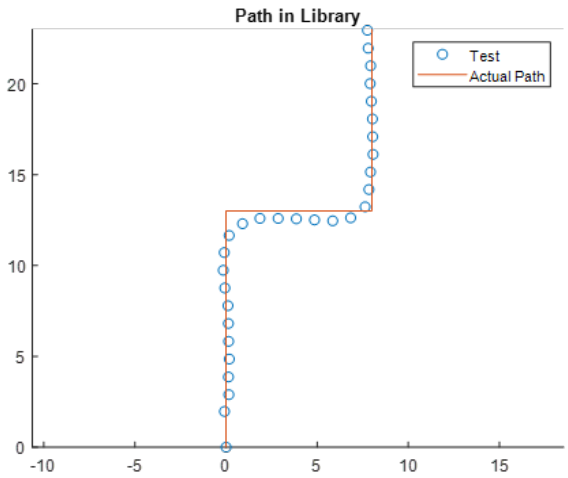

Figure 50. Path through AFIT Library

This is from an accurate translation vector as part of the pose matrix, of which attitude makes up the other half. The photos were taken by a student walking and holding the camera 3 feet in the air, but faced forward the whole time. The image matching process used SIFT and FLANN, with no outlier rejection of images. No timing data was necessary, but the points in Figure 50 are equally spaced, showing the images were taken at equal time steps assuming a constant velocity. When the

student takes the right turn, the camera experiences a 90° yaw, and would stay at that in Figure 51, if not for the second turn bringing the attitude back to the origin. There are ±10° of error, meaning when we suddenly apply this algorithm to a simulated satellite, there are going to be some growing pains.

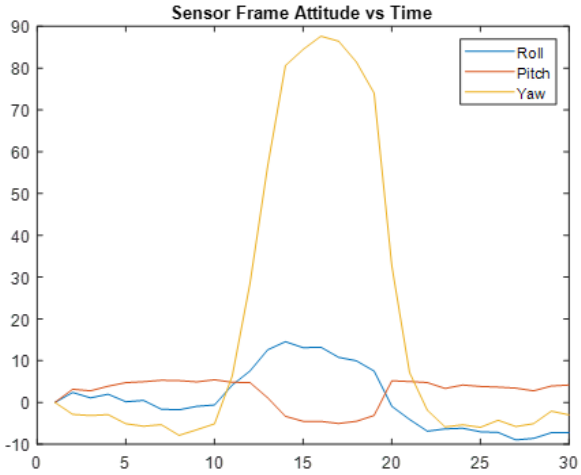

Figure 51. Attitude of Camera through AFIT Library

4.4.1 Test Length: Overland Nighttime Pass

Mode 2 of TIM involves testing two FOV images against each other, rather than to Black Marble, in a sequence of images. An example of TIM comparing two images from a test over the US is shown in Figure 52 and Figure 53. Figure 52 shows the results from Black Marbles images and 53 shows the measurements taken from Worldview of the same location. All images are assumed to be taken as the camera is aligned with the orbital frame.

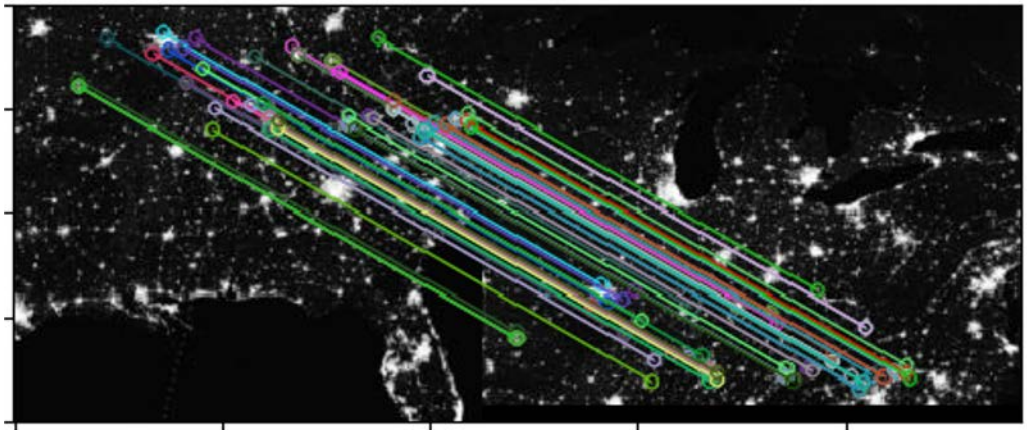

Figure 52. TIM Mode 2 in Operation over the Midwest, USA

The work of Lowe's ratio test can be seen in these images by looking at the slope and length of each line connecting a match. The slopes are all the same, and the relative distance between each match is also the same. Even where there are an abundance of matches, as shown in Figure 53, TIM is not connecting features in the images that are not genuine matches. Since this is a finer search than Mode 1, the strength of the match is much higher.

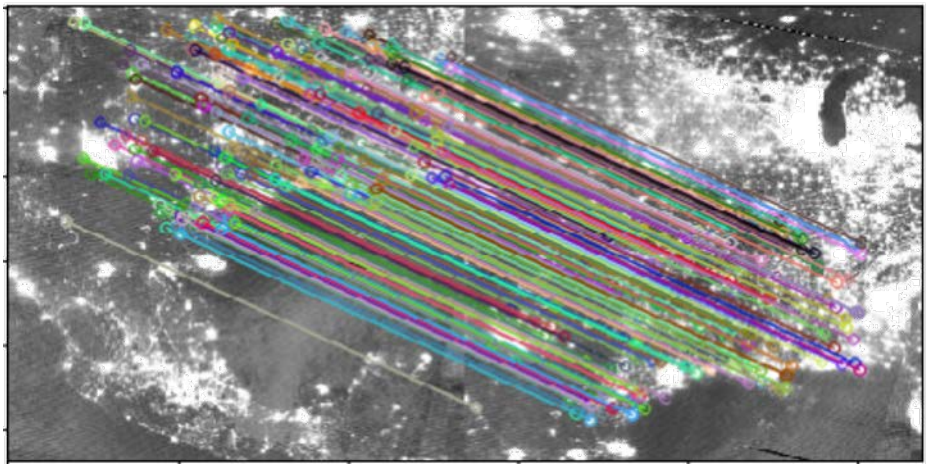

Figure 53. TIM Mode 2 in finding matches over the Midwest, USA

Given a scale of distance traveled between images based on Suomi NPP footprint coverage, a 3-component position estimate can be calculated from pose recovery,

which the norm of which would give altitude. The Woman data in Figure 54 was processed in an earlier version of TIM where the pose calculated from the Worldview image sequence was almost spot on, but did not correlate with the sequence from Black Marble. It is difficult to say if it was properly calculated or just a fluke that is was close to the altitude due to the disparity of Black Marble and Worldview results. When TIM was updated and the Veteran dataset processed, the image sequences from Black Marble and Worldview gave similar results, but were far from the truth. The results start at zero because the first image in the sequence has no information attached to it, and only the second and onwards in the sequence of images can give a pose estimate.

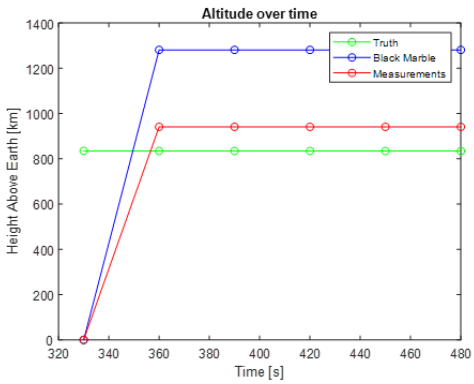

Figure 54. Woman Height Above Earth for Black Marble, Worldview (Meas)

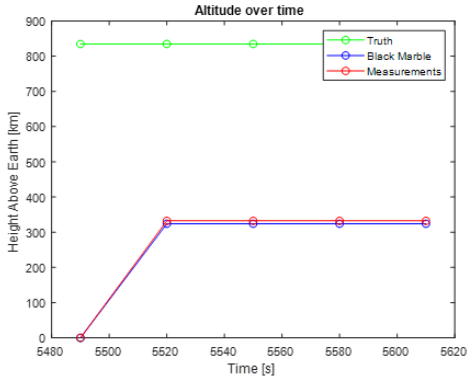

Figure 55. Veteran Height Above Earth for Black Marble, Worldview (Meas)

The Veteran data for roll, pitch and yaw, while not matching the truth, had relatively little error between what was calculated for the Black Marble and Measurements data. For the beginning of the Woman data, it also did well, but as time went on (meaning more images to process) the measurements yaw calculation jumped from negative to positive on the last image of the set.

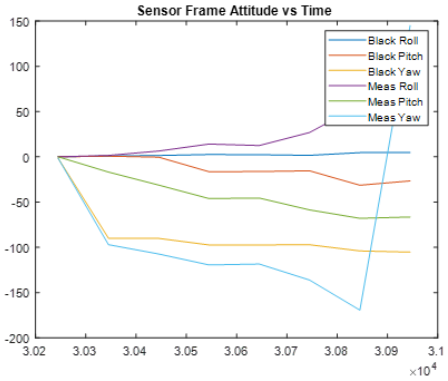

Figure 56. Woman Attitude in Euler Angles for Black Marble, Worldview (Meas)

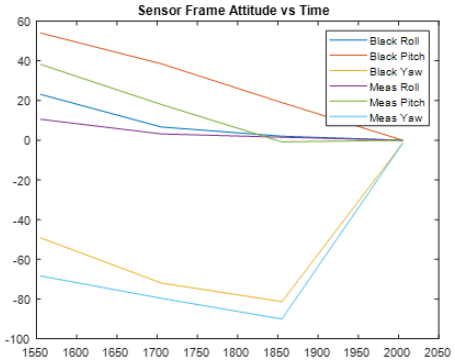

Figure 57. Veteran Attitude in Euler Angles for Black Marble, Worldview (Meas)

There are angle errors in roll in the real images because, when pulled from Worldview, the image was on a slant and not precisely acquired. This could be fixed by changing the image acquisition process for the simulation by using other raw data pulls from Suomi NPP rather than screenshots of Worldview. The altitude over time is also considerably off from expected values due to the small image set (the pose estimation improves with larger datasets) and problems with the algorithm are to be fixed in future work.

4.4.2 Summary

The attitude determination using this process does not share the same problems as position estimation. It is without any coordinate transformations, the attitude of the camera with reference to its first image is the attitude that is plotted in these figures. This suggests the scaling process could be at fault; it is suited for straight paths of travel and not a camera traveling in tiny hemispheres between image acquisition. Shorter time steps (10 seconds rather than 5 minutes) would overcome this and lead to better algorithm and filter function overall.

V. Conclusions and Recommendations

5.1 Conclusions of Research

This section will continue the discussion on using city lights for accurate position estimation during on-orbit operation. Keep in mind that this work contains preliminary results for position estimation that are the first attempt at such a capability. The work aims to show the feasibility of exploring this technology further by inventing methods to verify results and prepare for real-world conditions. Suomi NPP and the VIIRS instrument host a powerful suite of capability. The goal of this work is to use existing sensors to create novel navigation methods, with the intention of creating new dual-purpose and efficient sensors. Similar works have used landmark recognition with images from existing satellites, but typically struggle to get measurements for nighttime orbital passes. This research demonstrated the ability to find attitude change between images taken at night using city lights. The end goal of TIM is integrate the two modes and apply a Kalman filter. ORB is an algorithm that should be tested in the future, as well as exploring inverted images, Gaussian blurring, and thresholding. Finally, an EKF will be applied to estimate position and attitude in the event of measurements being unavailable due to daytime or extensive sea cover to be consistent with prior work. This will further be used to autonomously verify the success of Mode 1. Potential problems that will be discussed in future work are cloud cover and gaps in data collection, shown by the dark lines throughout the scans. As research progresses, different image processing challenges, such as color correction, distortion, sunlight, and thresholding will be explored [19,4]. Another goal of the work is to obtain the pose matrix fast enough to be used in a real mission. Vision-based sensors, whether for tracking urbanization and population densities in remote areas or for absolute positioning on landers, are becoming increasingly important [19].

Every avenue of capability must be explored as we continue to see the world in new ways.

5.2 Significance of Research

The first of its kind to use such a unique combination of tools to solve a navigation problem, this work transcended academic disciplines and caught the attention of many researchers. As we watch the development of the world where electricity comes to more sparse communities, this technology will only advance in accuracy.

Air Force Research Laboratories' Space Vehicle Directorate (AFRL/RV) awarded $40,000 in initial funding to explore this idea. A provisional patent was secured in January 2020, under the title "Aerospace Vehicle Navigation and Control System Comprising Terrestrial Illumination Matching Module for Determining Aerospace Vehicle Position and Attitude," and number 62/957,250 [38]. A conference paper was accepted on the basis of abstract review and presented at AIAA's Science and Technology Forum and Exposition in Orlando, Florida the same month [39]. Another conference paper was accepted on the basis of full paper review and presented at IEEE's Aerospace Conference in Big Sky, Montana in March [40].

5.3 Recommendations for Future Work

The following identifies potential recommendations for future development in various avenues in order of complexity:

Short-Term

- Real Time Video: TIM can be configured to operate on-board a camera while recording Black Marble or Worldview imagery. Black Marble or Worldview imagery can be printed for 2D operation, or applied to a globe for 3D operation.

A more advanced simulation of both can also be created on a computer. Camera set up can run real-time connected to another computer.

- Stereoscopic vision improvements: with better pose recovery and functionality of Mode 2, if possible a height above Earth can be determined from imagery. This can be done by exploring the scaling of these matrices, or different pose recovery techniques, such as Homography for point-to-point projection of 2D and 3D image points.

- OpenCV specifications: change conditions on SIFT, make Black Marble features pre-loadable so it does not have to recreate features every time a simulation is run.

- Thresholding: Usable data (day, night, clouds, unusable) can be thresholded by setting a DN that describes the pixel, and compared with historical data to see if it is normal for the pixel to be unusable or not. This will aid in computation time when speed is needed to improve over accuracy.

- Autonomous functionality: The ability to determine when a measurement update is needed for Mode 1 and to otherwise run Mode 2 to help the orbit's propagation scheme and also track precise attitude information.

- Kalman Filter: can be rewritten to handle latitude and longitude coordinates rather than an ECI coordinate rotated into a camera frame. UKF is most-likely a better fit but needs to find proper tuning values for appropriate operation.

Long-Term

- Real time video on a small satellite adapted computer

- Different orbits, resolutions, maneuvers

- Dynamic variance and sensitivity values
- Clouds and localized blackouts - summer months saturation problems
- Infrared rather than visible light and if unique composites can be made
- Artificial intelligence and neural networking capabilities in OpenCV
- Higher order filtering

Bibliography

[1] J. Wright, "Korean peninsula seen from space station," Feb 2014. Accessed on 2020-1-21.

[2] C. D. Elvidge, K. E. Baugh, M. Zhizhin, and F.-C. Hsu, "Why VIIRS data are superior to DMSP for mapping nighttime lights," *Proceedings of the Asia-Pacific Advanced Network*, 2013.

[3] C. C. Liebe, "Star trackers for attitude determination," *IEEE Aerospace and Electronic Systems Magazine*, vol. 10, no. 6, pp. 10–16, 1995.

[4] M. M. Birnbaum, "Spacecraft attitude control using star field trackers," *Acta Astronautica*, vol. 39, no. 9-12, pp. 763–773, 1996.

[5] M. Paluszek, M. Littman, and J. Mueller, "Optical Navigation System," *AIAA Infotech@Aerospace 2010*, no. April, 2010.

[6] L. D., "Distinctive Image Features from Scale-Invariant Keypoints," *International Journal of Computer Vision*, vol. 60, no. 2, pp. 91–110, 2004.

[7] H. Bay, T. Tuytelaars, and L. Van Gool, "SURF: Speeded Up Robust Features," *Computer Visiion: ECCV 2006 Berlin, Germany*, 2006.

[8] S. Leutenegger, M. Chli, and R. Siegwart, "BRISK: Binary Robust Invariant Scalable Keypoints," *2011 IEEE International Conference on Computer Vision (ICCV)*, pp. 2548–2555, 2011.

[9] E. Rublee, V. Rabaud, K. Konolige, and G. Bradski, "ORB: An efficient alternative to SIFT or SURF," *2011 International Conference on Computer Vision Barcelona*, pp. 2564–2571, 2011.

[10] E. Rosten, R. Porter, and T. Drummond, "Faster and Better: A Machine Learning Approach to Corner Detection," *IEEE Transactions on Pattern Analysis and Machine Intelligence*, vol. 32, pp. 105–119, Jan 2010.

[11] J. Matas, O. Chum, M. Urban, and T. Pajdla, "Robust Wide Baseline Sterero from Maximally Stable Extremal Regions," *Proc. of British Machine Vision Conference*, pp. 384–396, 2002.

[12] M. Calonder, V. Lepetit, C. Strecha, and P. Fua, "BRIEF: Binary Robust Independent Elementary Features," *European Conference on Computer Vision EECV*, vol. 6214, pp. 778–792, 2010.

[13] A. Alahi, R. Ortiz, and P. Vandergheynst, "FREAK: Fast Retina Keypoiny," *2012 IEEE Conference on Computer Vision and Pattern Recognition, Providence, RI*, pp. 510–517, 2012.

[14] "OpenCV: Feature Matching." Accessed 18 Feb. 2019.

[15] L. D. Muja, M., "Scalable Nearest Neighor Algorithms for High Dimensional Data," *IEEE Transactions on Pattern Analysis and Machine Intelligence*, vol. 52, no. 1, pp. 1–14, 2007.

[16] M. A. Fischler and R. C. Bolles, "Random Sample Consensus: A Paradigm for Model Fitting with Applications to Image Analysis and Automated Cartography," *Communications of the Association for Computing Machinery*, vol. 24, no. 6, pp. 381–395, 1981.

[17] R. Siegwart, I. R. Nourbakhsh, and D. Scaramuzza, "Autonomous mobile robots," *A Bradford Book*, 2011.

[18] M. M. Veth and J. Raquet, "Fusing low-cost image and inertial sensors for passive Navigation," *Navigation, Journal of the Institute of Navigation*, vol. 54, no. 1, pp. 11–20, 2007.

[19] M. J. Veth, "Navigation using images, a survey of techniques," 2011.

[20] C. D. Elvidge, K. E. Baugh, E. A. Kihn, and H. W. Kroehl, "Mapping City Lights with Nighttime Data from the DMSP Operational Linescan System," *Photogrammetric Engineering and Remote Sensing*, vol. 63, no. 6, pp. 727–734, 1997.

[21] United States Department of the Air Force, "Air Force Instruction 11-202V3 General Flight Rules," August 2016. Updated October 2019.

[22] K. Baugh, C. D. Elvidge, T. Ghosh, and D. Ziskin, "Development of a 2009 Stable Lights Product using DMSP-OLS data," *Proceedings of the Asia-Pacific Advanced Network*, 2010.

[23] D. Hilliger, "First-Light Imagery from Suomi NPP VIIRS," *Bulletin of the American Meteorological Society*, vol. 94, pp. 1019–1029, 2013.

[24] SAIC under contract to CFSCC CJ3/6 to USSPACECOM.

[25] C. Cao, "NOAA Technical Report NESDIS 142 Visible Infrared Imaging Radiometer Suite (VIIRS) Sensor Data Record (SDR) User s Guide," no. March, 2017.

[26] "NASA Earth Observing System Data and Information System (EOSDIS)." Accessed 18 Oct. 2019.

[27] Román, Miguel O., et alia, "NASA's Black Marble nighttime lights product suite," *Remote Sensing of Environment*, vol. 210, no. November 2017, pp. 113–143, 2018.

[28] J. Checa and O. Nel·lo, "Urban Intensities. The Urbanization of the Iberian Mediterranean Coast in the Light of Nighttime Satellite Images of the Earth," *Urban Science*, vol. 2, no. 4, p. 115, 2018.

[29] M. Imhoff, W. T. Lawrence, C. D. Elvidge, and N. Oceanic, "A technique for using composite DMSP / OLS City Lights satellite data to map urban area," vol. 4257, no. September, 1997.

[30] S. Amaral, A. M. Monteiro, G. Camara, and J. A. Quintanilha, "DMSP/OLS night-time light imagery for urban population estimates in the Brazilian Amazon," *International Journal of Remote Sensing*, vol. 27, no. 5, pp. 855–870, 2006.

[31] G. Klancar, S. Blažic, D. Matko, and G. Mušic, "Image-based attitude control of a remote sensing satellite," *Journal of Intelligent and Robotic Systems: Theory and Applications*, vol. 66, no. 3, pp. 343–357, 2012.

[32] M. N. Straub and J. A. Christian, "Autonomous Optical Navigation for Earth-Observing Satellites Using Coastline Matching," no. January, pp. 1–10, 2015.

[33] T. Kouyama, A. Kanemura, S. Kato, N. Imamoglu, and T. Fukuhara, "Satellite Attitude Determination and Map Projection Based on Robust Image Matching," pp. 1–20, 2017.

[34] D. A. Vallado, *Fundamentals of astrodynamics and applications*, vol. 12. Springer Science & Business Media, 2001.

[35] B. L. Stevens, F. L. Lewis, and E. N. Johnson, "The kinematics and dynamics of aircraft motion," 2015.

[36] R. F. Stengel, *Optimal control and estimation*. Courier Corporation, 1994.

[37] J. L. Crassidis and J. L. Junkins, *Optimal estimation of dynamic systems*. Chapman and Hall/CRC, 2011.

[38] L. M. Shockley and R. A. Bettinger, "Aerospace vehicle navigation and control system comprising terrestrial illumination matching module for determining aerospace vehicle position and attitude," *U.S. Provisional Patent*, January 2020.

[39] L. M. Shockley and R. A. Bettinger, "Spacecraft position estimation using terrestrial illumination matching," *2020 AIAA Science and Technology Forum and Exposition, Orlando, FL*, January 2020.

[40]

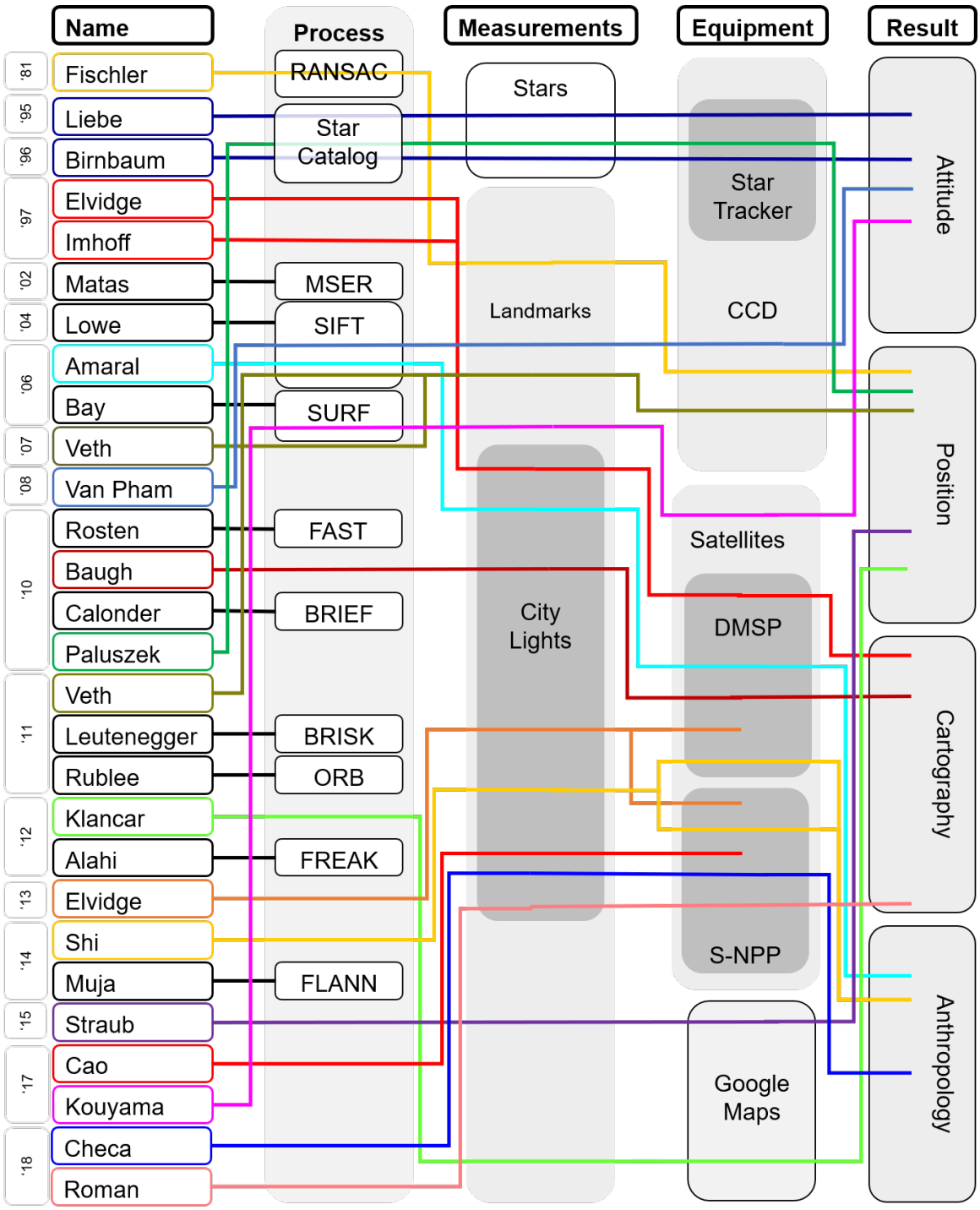
Name
Process
Measurements
Equipment
Result
'81
'95
'96
'97
'02
'04
'06
'07
'08
'10
'11
'12
'13
'14
'15
'17
'18
Fischler
Liebe
Birnbaum
Elvidge
Imhoff
Matas
Lowe
Amaral
Bay
Veth
Van Pham
Rosten
Baugh
Calonder
Paluszek
Veth
Leutenegger
Rublee
Klancar
Alahi
Elvidge
Shi
Muja
Straub
Cao
Kouyama
Checa
Roman
RANSAC
Star Catalog
MSER
SIFT
SURF
FAST
BRIEF
BRISK
ORB
FREAK
FLANN
Stars
Landmarks
City Lights
Star Tracker
CCD
Satellites
DMSP
S-NPP
Google Maps
Attitude
Position
Cartography
Anthropology

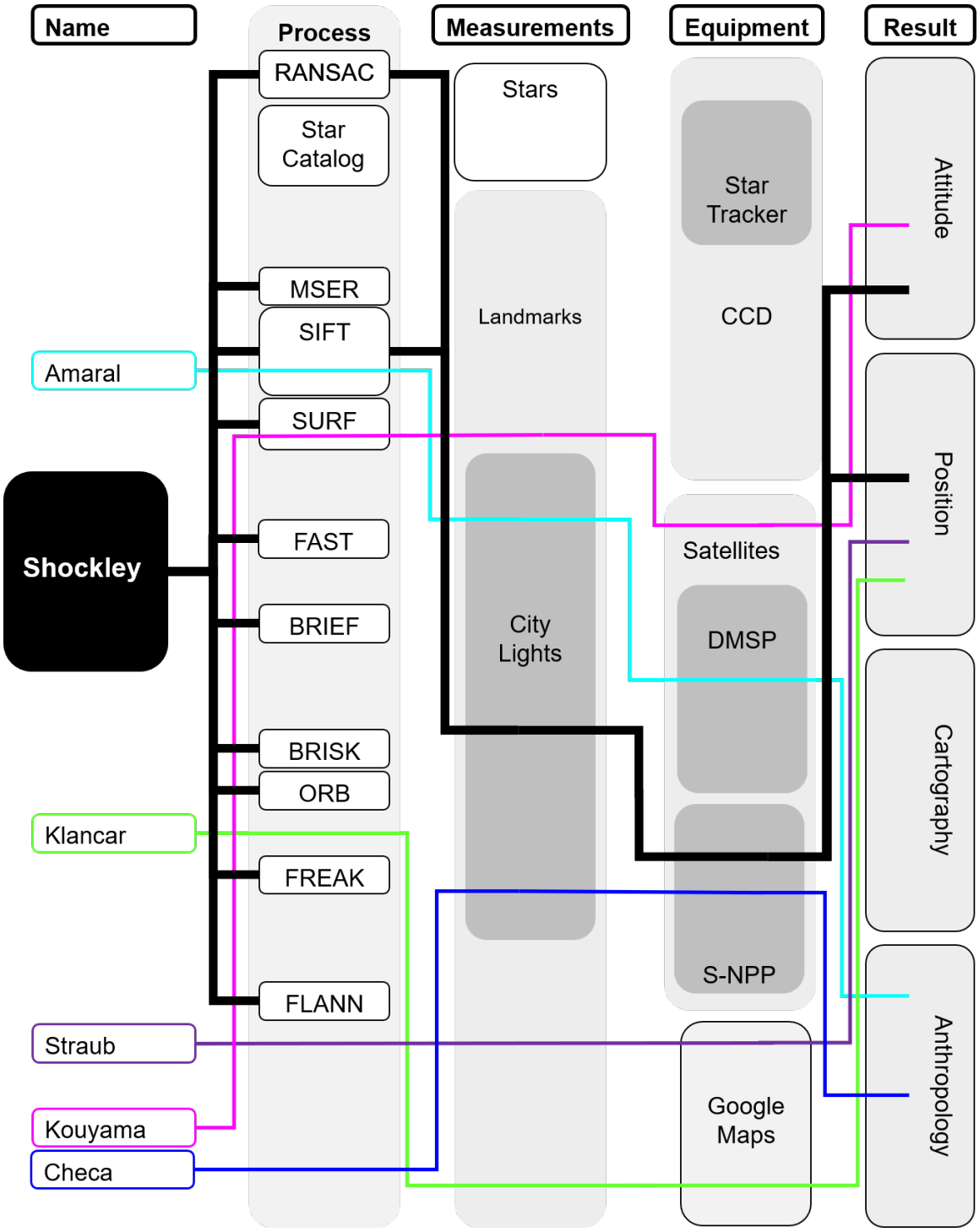
Name
Process
Measurements
Equipment
Result
RANSAC
Star Catalog
MSER
SIFT
SURF
FAST
BRIEF
BRISK
ORB
FREAK
FLANN
Shockley
Amaral
Klancar
Straub
Kouyama
Checa
Stars
Landmarks
City Lights
Star Tracker
CCD
Satellites
DMSP
S-NPP
Google Maps
Attitude
Position
Cartography
Anthropology

Vita

2nd Lieutenant Liberty M. Shockley is originally from Oklahoma but graduated from Beavercreek High School in Ohio after 17 years living all over the world as an Air Force Brat. She was awarded a prestigious scholarship from the United States Air Force to attend the University of Cincinnati College of Engineering and Applied Science where she studied Aerospace Engineering. During this time, Lt Shockley worked at NASA Goddard Space Flight Center in Greenbelt, Maryland over two semesters, first working on in-house developed star tracker attitude algorithms, and then as an engineer supporting a big bang cosmology balloon experiment. She spent her breaks teaching English in Nepal, and the State Department awarded her a military scholarship to study Hindi while living in Varanasi, India on her summer break. This was instrumental to Lt Shockley's development as a global citizen, now speaking Nepali, Hindi, and Levantine Arabic, and enjoys studying these regions when her head isn't out in space. While in school she worked as an undergraduate research assistant on path-planning navigation algorithms to air firefighters in fire detection and missing persons searches. She also helped submit two Small Business Innovation Research proposals (SBIR) for high-altitude unmanned aerial vehicles. Despite all this activity, she was able to graduate a year ahead of her peers.

After commissioning, Lt Shockley's first assignment was to the Graduate School of Engineering and Management at the Air Force Institute of Technology (AFIT) which is special to her, as her father received his Masters and PhD in Electrical Engineering from AFIT. Following completion of the Astronautical Engineering Masters program she will be assigned as a Satellite Test Flight Engineer to Space and Missiles Command (SMC) at Kirtland AFB, New Mexico. Lt Shockley has been accepted to the Astronautical Engineering Doctoral program at AFIT and will continue this work until she is able to return to complete her PhD (and hopefully then can go be an astronaut).

REPORT DOCUMENTATION PAGE

Form Approved
OMB No. 0704-0188

1. REPORT DATE *(DD-MM-YYYY)*	**2. REPORT TYPE**	**3. DATES COVERED** *(From - To)*
03/26/2020	Master's Thesis	September 2018 - March 2020

4. TITLE AND SUBTITLE
Spacecraft Position Estimation and Attitude Determination using Terrestrial Illumination Matching

5a. CONTRACT NUMBER

5b. GRANT NUMBER

5c. PROGRAM ELEMENT NUMBER

6. AUTHOR(S)
Shockley, Liberty M., Second Lieutenant, USAF

5d. PROJECT NUMBER

5e. TASK NUMBER

5f. WORK UNIT NUMBER

7. PERFORMING ORGANIZATION NAME(S) AND ADDRESS(ES)
Air Force Institute of Technology
Graduate School of Engineering and Management (AFIT/ENY)
2950 Hobson Way, Building 640
WPAFB OH 45433-8865

8. PERFORMING ORGANIZATION REPORT NUMBER
AFIT-ENY-MS-20-M-280

9. SPONSORING/MONITORING AGENCY NAME(S) AND ADDRESS(ES)
Air Force Research Labs Space Vehicles
2550 Aberdeen Ave SE, Bldg 427
Kirtland AFB, NM 87117-5776

10. SPONSOR/MONITOR'S ACRONYM(S)
AFRL/RV

11. SPONSOR/MONITOR'S REPORT NUMBER(S)
N/A

12. DISTRIBUTION/AVAILABILITY STATEMENT
DISTRIBUTION STATEMENT A.
Approved for Public Release; Distribution is Unlimited

13. SUPPLEMENTARY NOTES
The material is declared a work of the U.S. Government and is not subject to copyright protected in the United States

14. ABSTRACT
An algorithm to conduct spacecraft position estimation and attitude determination via terrestrial illumination matching (TIM) is presented consisting of a novel method that uses terrestrial lights as a surrogate for star fields. Although star sensors represent a highly accurate means of attitude determination with considerable spaceflight heritage, with Global Positioning System (GPS) providing position, TIM provides a potentially viable alternative in the event of star sensor or GPS malfunction or performance degradation. The research defines a catalog of terrestrial light "constellations," which are then implemented within the TIM algorithm for position acquisition of a generic spacecraft bus.

15. SUBJECT TERMS
terrestrial illumination matching; terrestrial lights; position estimation; attitude determination; satellite navigation; spacecraft navigation

16. SECURITY CLASSIFICATION OF:			**17. LIMITATION OF ABSTRACT**	**18. NUMBER OF PAGES**	**19a. NAME OF RESPONSIBLE PERSON**
a. REPORT	**b. ABSTRACT**	**c. THIS PAGE**			Robert Bettinger, Maj, USAF
					19b. TELEPHONE NUMBER *(Include area code)*
UU	UU	UU	UU	78	(937) 255-6565, ext 4578

INSTRUCTIONS FOR COMPLETING SF 298

1. REPORT DATE. Full publication date, including day, month, if available. Must cite at least the year and be Year 2000 compliant, e.g. 30-06-1998; xx-06-1998; xx-xx-1998.

2. REPORT TYPE. State the type of report, such as final, technical, interim, memorandum, master's thesis, progress, quarterly, research, special, group study, etc.

3. DATE COVERED. Indicate the time during which the work was performed and the report was written, e.g., Jun 1997 - Jun 1998; 1-10 Jun 1996; May - Nov 1998; Nov 1998.

4. TITLE. Enter title and subtitle with volume number and part number, if applicable. On classified documents, enter the title classification in parentheses.

5a. CONTRACT NUMBER. Enter all contract numbers as they appear in the report, e.g. F33315-86-C-5169.

5b. GRANT NUMBER. Enter all grant numbers as they appear in the report. e.g. AFOSR-82-1234.

5c. PROGRAM ELEMENT NUMBER. Enter all program element numbers as they appear in the report, e.g. 61101A.

5e. TASK NUMBER. Enter all task numbers as they appear in the report, e.g. 05; RF0330201; T4112.

5f. WORK UNIT NUMBER. Enter all work unit numbers as they appear in the report, e.g. 001; AFAPL30480105.

6. AUTHOR(S). Enter name(s) of person(s) responsible for writing the report, performing the research, or credited with the content of the report. The form of entry is the last name, first name, middle initial, and additional qualifiers separated by commas, e.g. Smith, Richard, J, Jr.

7. PERFORMING ORGANIZATION NAME(S) AND ADDRESS(ES). Self-explanatory.

8. PERFORMING ORGANIZATION REPORT NUMBER. Enter all unique alphanumeric report numbers assigned by the performing organization, e.g. BRL-1234; AFWL-TR-85-4017-Vol-21-PT-2.

9. SPONSORING/MONITORING AGENCY NAME(S) AND ADDRESS(ES). Enter the name and address of the organization(s) financially responsible for and monitoring the work.

10. SPONSOR/MONITOR'S ACRONYM(S). Enter, if available, e.g. BRL, ARDEC, NADC.

11. SPONSOR/MONITOR'S REPORT NUMBER(S). Enter report number as assigned by the sponsoring/ monitoring agency, if available, e.g. BRL-TR-829; -215.

12. DISTRIBUTION/AVAILABILITY STATEMENT. Use agency-mandated availability statements to indicate the public availability or distribution limitations of the report. If additional limitations/ restrictions or special markings are indicated, follow agency authorization procedures, e.g. RD/FRD, PROPIN, ITAR, etc. Include copyright information.

13. SUPPLEMENTARY NOTES. Enter information not included elsewhere such as: prepared in cooperation with; translation of; report supersedes; old edition number, etc.

14. ABSTRACT. A brief (approximately 200 words) factual summary of the most significant information.

15. SUBJECT TERMS. Key words or phrases identifying major concepts in the report.

16. SECURITY CLASSIFICATION. Enter security classification in accordance with security classification regulations, e.g. U, C, S, etc. If this form contains classified information, stamp classification level on the top and bottom of this page.

17. LIMITATION OF ABSTRACT. This block must be completed to assign a distribution limitation to the abstract. Enter UU (Unclassified Unlimited) or SAR (Same as Report). An entry in this block is necessary if the abstract is to be limited.